Particle Accelerators, 1995, Vol. 49, pp. 27–65
Reprints available directly from the publisher
Photocopying permitted by license only

© 1995 OPA (Overseas Publishers Association)
Amsterdam B.V. Published under license by
Gordon and Breach Science Publishers SA
Printed in Malaysia

SPACE-CHARGE-INDUCED EMITTANCE COMPENSATION IN HIGH-BRIGHTNESS PHOTOINJECTORS*

BRUCE E. CARLSTEN

Los Alamos National Laboratory, Los Alamos, NM 87545 USA

(Received 28 April 1994; in final form 21 September 1994)

We have developed an emittance compensation scheme for the space-charge-induced emittance growth in high-brightness electron beams. This technique has been incorporated in 1.3 GHz photoinjector experiments at Los Alamos National Laboratory by introducing solenoidal focusing near the photocathode. Other laboratories are using or contemplating using the scheme for photoinjectors ranging from 108 MHz to 2.856 GHz. In our experiments, this scheme has consistently reduced the normalized rms emittance by up to an order of magnitude over what it would be without compensation. In this paper, we explain how this scheme works and discuss the physics leading to the residual emittance after compensation. We additionally present a numerical model of the technique which leads to universal scaling curves for predicting the residual emittance as a function of beam current, accelerating gradient and other conditions, and show that experimental data from the Los Alamos Advanced Prototype EXperiment (APEX) free-electron laser facility is consistent with these results. These scaling curves can be used to determine optimum photoinjector conditions for desired electron bunch parameters.

KEY WORDS: Beam transport, electron beam devices, injectors, particle dynamics

1 INTRODUCTION

A simple scheme has been developed[1] that decreases the rms emittance of low-emittance, high-charge electron bunches by up to an order of magnitude. This technique is especially suited for reducing the space-charge-induced emittance growth in photoinjectors. This emittance compensation scheme has two important features: (1) use of this scheme minimizes the final normalized rms emittance at the end of the beam line and (2) the normalized rms emittance actually monotonically decreases for a while as the beam travels down the beam line after the initial large emittance growth near the photocathode and before the beam becomes relativistic. By proper design, an emittance minimum can be placed at any arbitrary high energy. This decrease in the normalized rms emittance as the beam travels in the accelerator does not violate Liouville's theorem and is accomplished simply by exploiting the correlations in the beam's six-dimensional phase space. In general,

*Work supported by the Los Alamos Laboratory Directed Research and Development program, under the auspices of the US Department of Energy.

this technique can be used to modify an undesirable phase-space distribution of dimension less than n with large correlations caused by a nonlinear force in a Hamiltonian system of dimension n. (Once the distribution thermalizes and the correlations disappear, this technique will no longer work.) The advantage of this technique is that it is simple to apply because it only requires a linear force that is not a function of time. In the case of a photoinjector, this linear force is supplied by a simple solenoid. Crucial issues associated with the use of this scheme are (1) what is the residual emittance after compensation and (2) how can the compensation be improved. Unfortunately, these questions cannot be adequately answered by detailed numerical simulations of the particles' motion in the photoinjector because the residual emittance is a complex function of several independent photoinjector parameters and is often masked by the rf-induced emittance. The full potential of the compensation scheme can only be realized if there is a simple model presenting clear scalings for the residual emittance. The purpose of this paper is to describe the compensation technique, discuss the physics associated with the residual emittance after compensation, and present normalized scaling curves showing the residual emittance as a function of the compensation parameters and the accelerating gradient for short-pulse (high-current) photoinjectors. We predict that the compensation is better for conditions maximizing the beam laminarity and that the residual emittance is minimized by operating at a specific cathode current density which is given as a function of the gradient. Finally, we show that the compensation model is consistent with the most complete published set of photoinjector rms emittance measurements to date.

Many effects can create transverse emittance growth in bright, relativistic electron beams. The emittance growth contributions from the space-charge and rf fields are inherent in an accelerated electron bunch and do not arise from misalignments and other errors. In addition, there are other effects which are not fundamental limitations and appear as a result of construction tolerances or error and operation error. These effects include rotated quadrupole magnets, beam transverse offsets leading to transverse wakefields, and non-achromatic bends.[2] Because these effects are typically uncorrelated, we expect that the emittance contributions from each source add in quadrature. Carefully designing the rf cavities, all space harmonics above the fundamental vanish, and the rf field is radially linear.[3] For this case, Kim[4] has explicitly calculated the emittance growth from the time-dependent, radially linear rf fields in a photoinjector by directly integrating the transverse force equation from the rf fields. We can define the transverse emittance to be

$$\varepsilon_{x,n} = \beta\gamma\sqrt{\langle x^2\rangle\langle x'^2\rangle - \langle xx'\rangle^2}\,, \tag{1}$$

where β is the axial velocity divided by the speed of light, γ is the relativistic mass factor, $x' = dx/dz$, and the angled brackets refer to ensemble averages over the particle distribution. The emittance is the rms area that the beam occupies in the $x - x'$ phase space divided by π. Using common convention, however, we will quote emittance numbers with the units π mm mrad, which is the area in phase space. Kim has shown that the rf-induced transverse emittance growth for an electron bunch of negligible charge with a Gaussian distribution, with rms transverse bunch length σ_x and rms longitudinal bunch length σ_z, in a photoinjector with an rf field amplitude E_o and wave number k, can be written as

$$\varepsilon_{x,n} = \frac{eE_o}{2\sqrt{2}m_o c^2} k^2 \sigma_x^2 \sigma_z^2 \tag{2}$$

where e and m_o are the electronic charge and mass respectively. We see that the emittance contribution decreases as the longitudinal bunch length decreases but increases with both increasing frequency or gradient. The instantaneous emittance growth contribution depends on the square of the transverse beam size at that moment. Thus, the transverse emittance growth from the rf fields must also depend on the bunch's radial expansion from the space-charge forces, which is not included in Eq. (2). However, Eq. (2) is still valid in the low-current regime and demonstrates the scaling of the emittance to the beam size.

Determining the emittance growth from the space-charge forces is not as straightforward as that from the rf forces. Scaling arguments, confirmed by particle-in-cell simulations, show that the transverse emittance growth for a drifting slug of length L and radius a with peak current I obeys[5]

$$\varepsilon_{x,n} = \frac{eIs}{16\pi\varepsilon_o m_o c^3 \gamma^2 \beta^2} G(\gamma L/a) \tag{3}$$

as long as the slug does not appreciably deform over the drift distance s. The geometric factor G depends on the beam's aspect ratio in its own frame of reference and the longitudinal distribution. G can be calculated for distributions in the long-bunch limit by using Gauss' law to find the radial electric field. For beams with uniform radial distributions in this limit, G is 0.556 if the longitudinal distribution is Gaussian, 0.236 if it is triangular, and 0.214 if it is parabolic. Because the rf-induced emittance growth depends on the beam current it is hard to differentiate between the rf-induced and the space-charge-induced emittance growths, both in experiments and numerical simulations.

The inverse scaling with beam energy in Eq. (3) indicates that it is desirable to accelerate an electron bunch quickly. Photocathodes within rf cavities, known as photoinjectors, have been developed that provide immediate acceleration when the electrons are drawn off the cathode in MV/m-type axial electric fields.[6–9] Kim has additionally integrated Eq. (3) to determine the emittance growth from the photoinjector's space-charge forces.[4] His results agree relatively well with some experiments.[4] In principle, Kim's equations for the emittance growth from rf and space-charge fields can be used to determine the bunch length and radius that minimize the emittance for a given charge. However, in practice this is not done because peak current is often more important than bunch charge. The space-charge-induced emittance growth (Eq. (3)) is often much larger than the rf-induced emittance growth (Eq. (2)), especially for bunch charges greater than 1 nC in relatively low frequency (and thus low gradient) photoinjectors.

Significantly smaller transverse beam emittances have been measured for L-band photoinjectors than predicted by Kim's formulae[7,8,10] (by factors up to ten). Los Alamos National Laboratory developed a novel emittance compensation technique to do this. The technique uses an external solenoid around the photoinjector and is described in this paper in detail. In particular, we will present simplified models of how this compensation works, discuss the physics associated with the residual emittance after compensation, and actually calculate normalized universal scaling curves for the residual emittance that can be used for photoinjector design. This is an important issue because slight variations in either the beam or

compensation parameters can increase the residual emittance by factors of two or more. We first present two simplified analytic models for this phenomena. These models crudely demonstrate the essential physics of the compensation in both the short-beam and long-beam regimes. The model in the long-beam regime leads to a picture of how the residual emittance forms. We find that the residual emittance results from the nonlinear terms in the axial Taylor expansion of the radial space-charge force. Unfortunately, this model cannot be conveniently extended to estimate the residual emittance for actual photoinjectors, so we build a numerical model from the essential elements found in the analytic models to study this effect under conditions of acceleration in a photoinjector, and then calculate the residual emittance from the space-charge forces. We assume that the beam is long enough that the electric field is primarily radial. The errors associated with this assumption are discussed. Qualitative agreement is found between the crude long-beam model and the numerical results. We present scaling arguments, which lead to universal curves showing both this compensation and also the residual emittance from the space-charge forces as a function of the accelerating gradient and the cathode current density. Contrary to Eq. (3), we find that a higher accelerating gradient does not always lead to a lower emittance. In both the analytic model and the numerical simulations, we find that the residual emittance is minimized if the beam laminarity is maintained. In addition, we examine experimental emittance results from a compensated photoinjector. The measured emittances include the rf-induced component, which brings in additional complexity and makes a direct measurement of the residual space-charge-induced emittance difficult. However, we are able to derive from physical arguments a form for the emittance which includes both the rf-induced and space-charge-induced emittances. After fitting the unknown constants in the part of the formula for the rf-induced emittance growth, we show that the quantitative results for the residual emittance are consistent with the measurements.

In Section 2, we present the analytic models describing the compensation technique. In Section 3, we discuss the numerical model for a long beam in a constant accelerating field. Universal compensation curves are given in Section 4, along with estimates for the uncompensated bunch emittance. In Section 5, we compare the compensation measured experimentally to Kim's formulae and to the universal curves.

2 ANALYTIC MODELS OF COMPENSATION

The purpose of this section is to present the necessary physics to understand both the compensation technique and the cause of the residual emittance after compensation. In particular, the conclusions from this section will be used to justify the use of the numerical model of the residual emittance presented in Section 3. This will be done by understanding what physics must be included to calculate the residual emittance. A second purpose of this section is to qualitatively predict some features to compare with the results from the numerical model. First, we present two simplified models for the compensation that demonstrate the important physics. The essential features that these models must show include (1) an emittance growth before the lens, (2) a monotonic reduction in the emittance after the lens up to the location of an emittance minimum, and (3) some mechanism for describing the residual emittance, if any. We next discuss the bunch dynamics in

a photoinjector and see that for typical short-pulse photoinjectors the beam, in its own relativistic frame of reference, is initially short (relative to its radius) and becomes long as it is accelerated. We see that there is space-charge-induced emittance growth in both the short- and long-bunch regimes and see that the beam physics in each regime is represented by one of the models previously presented. The first model predicts that the residual emittance generated while the beam is short vanishes. The second model predicts that the residual emittance from the long-bunch regime is due to beam nonlaminarities and in general does not vanish. We also present a detailed numerical simulation of the compensation for an accelerated bunch in an actual L-band photoinjector and show that the residual emittance is primarily due to forces in the long-beam regime by direct inspection of the phase-space plots. Using this analysis, we see that the residual emittance can be estimated by simulating only the long-bunch physics, which we will numerically do in Section 3.

The radial space-charge force in a bunch is a function of position within the bunch. We can define an internal cylindrical coordinate system ρ and ζ to indicate different points in a slug beam. Let $\rho = 1$ define the radial edge and $\zeta = \pm 1$ define the axial ends. No emittance growth would result from the space-charge forces if the space-charge force is linear in ρ and independent of ζ:

$$\Lambda(\rho, \zeta, t) = \frac{eE_r(\rho, \zeta, t)}{m_o \gamma^3 \beta^2 c^2} = \rho \Lambda_o(t) \,, \tag{4}$$

where Λ is the force conveniently normalized and E_r is the radial electric field in the laboratory frame. This is not true in general, however, and the emittance grows as the beam either drifts or accelerates in an rf cavity. The emittance that develops has no chance to thermalize in a photoinjector; as a result the beam's phase space has a relatively large surface area but a small volume. Consider a bunch with a smooth longitudinal charge distribution that is zero at the ends of the bunch and is peaked at the bunch's center and a uniform radial distribution. If the bunch is long enough that the electric field is essentially radial, the transverse emittance scribed out by the beam's transverse phase space looks like a rotated bow tie, Fig. 1. In any axial slice of the beam, the emittance vanishes but

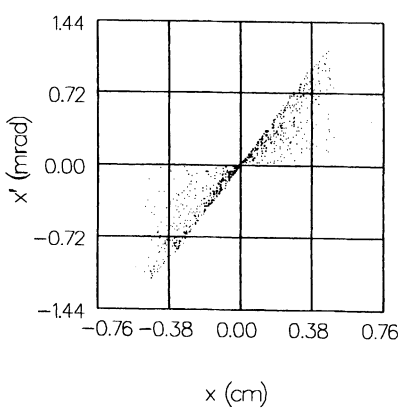

FIGURE 1: Typical phase-space bow tie formed by drifting beam.

it can be quite large when integrated axially over the bunch. In fact, the phase-space line corresponding to an axial slice of the beam rotates in phase space, first towards the x' axis and then back to the x axis as we move from one end of the bunch to another. We will refer to the axially integrated emittance as the rms emittance. For certain applications (e.g., free-electron laser[8]), the emittance of a single slice is more important than the rms emittance, while for other applications (e.g., minimizing beam interception) the rms emittance is more important. Additionally, if the bunch is magnetically compressed, the slices mix and the slice emittance approaches the rms emittance.

The emittance will vanish if we differentially rotate the phase-space lines corresponding to the different axial beam slices so that they all lie at the same angle. Note that this does not violate Liouville's theorem, which requires that only the 6-D phase-space density remains constant. The x emittance is simply a 2-D projection of this 6-D distribution, and no general conservation law applies. It would be easy to make the emittance vanish if we had a lens with which we could vary the focal length on the time scale of the bunch length. A cavity's rf fields could generate a lens which operates on a short time scale.[11,12] However, since the bunch is much shorter than the rf period, we would not expect to reduce the emittance significantly by using this type of technique. On the other hand, the compensation scheme using the external solenoid does exactly that, as we will see in the next subsections.

2.1 *Simplified Analytic Model of Compensation Using Constant Force Approximation*

In this subsection we introduce a crude model of a drifting beam under the influence of transverse space-charge forces and a linear focusing lens. The purpose of this model is to demonstrate that under certain conditions we can expect the emittance growth to totally vanish by using this compensation scheme. In the following subsection we introduce another model in which we show that only the emittance growth from the part of the nonlinear force which can be written as a first-order axial Taylor expansion vanishes. The emittance compensation scheme we discuss here and in the next subsection uses the nonlinear space-charge forces after a time-independent lens to remove phase-space correlations which were introduced by the nonlinear space-charge forces before the lens. The purpose of the lens is to rotate the entire phase-space distribution so that this compensation will happen. Consider the phase-space plots in Fig. 2 where we explicitly track the orbits for a particle at $(\rho, \zeta) = (1, 0)$ (at the axial center of the bunch) and one at (1,1) (at an axial end of the bunch). The curved lines with the arrows in the plots represent the phase-space orbits of the particles and the straight lines define the phase-space region occupied by the beam. The bow tie is formed from axial nonlinearities as the beam is drifted. An external lens rotates the distribution. Then as the beam drifts further, the slices rotate differently in phase space. If the lens conditions are correct, all slices rotate to exactly the same angle at some drift distance, and the initial emittance growth has been compensated.

To see how this is possible let us consider a drifting slug beam. Let us assume for this model that the space-charge force does not vary with time (the next model will be less restrictive). Then, with an initial nondivergent beam of radius r_o, a point in the slug given by (ρ, ζ) will obey non relativistic transverse motion:

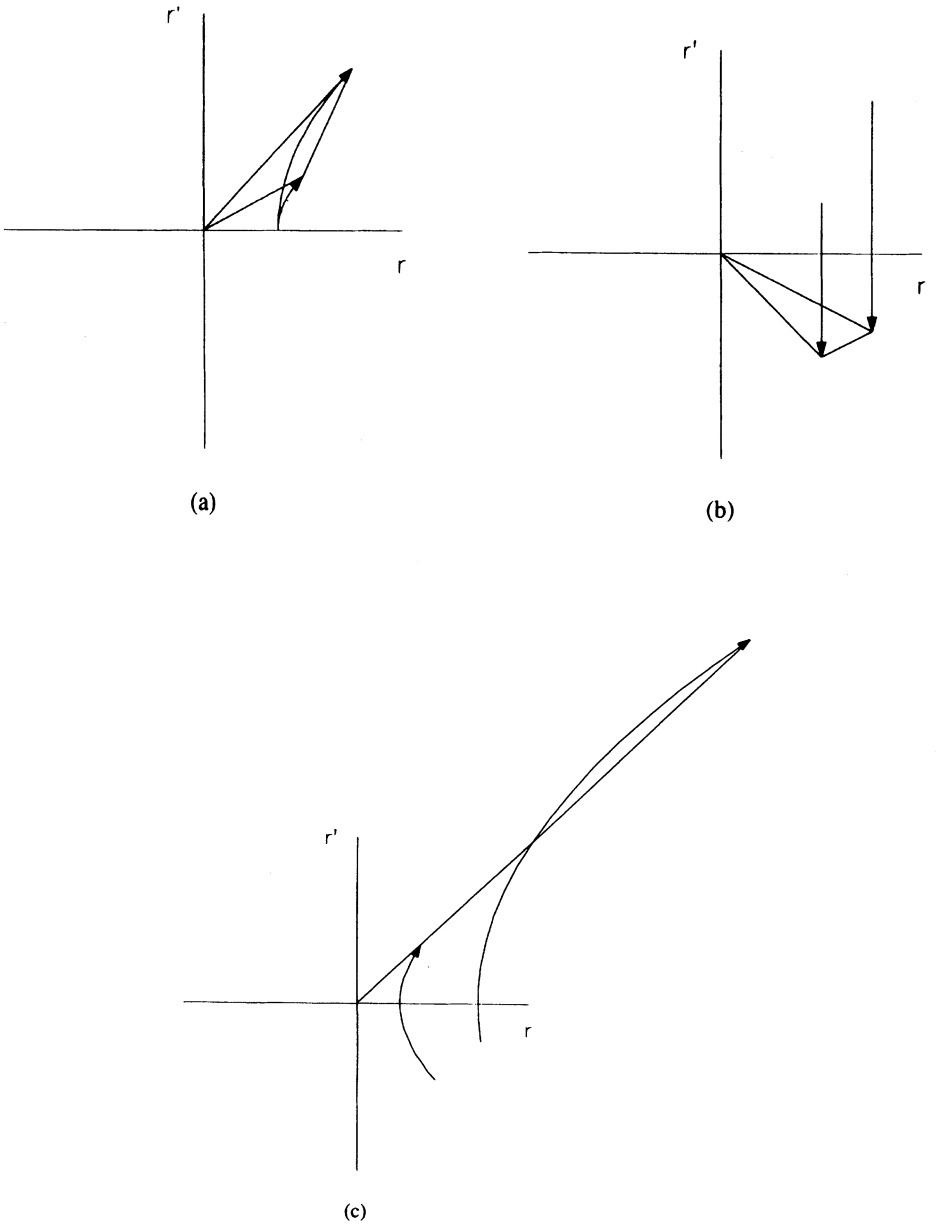

FIGURE 2: Phase-space orbits for particles along the beam's radial edge (one at the axial center of the bunch and one at an end), and the resulting bow ties defined by these trajectories.
(a) Particle orbits as the initially nondivergent beam drifts to the lens.
(b) Particle orbits within the lens.
(c) Particle orbits as the beam drifts after the lens. Note that the bow tie collapses as the orbits progress.

$$r(\rho,\zeta) = \rho r_o + \Lambda(\rho,\zeta)\frac{z^2}{2} \tag{5}$$

and

$$r'(\rho,\zeta) = \Lambda(\rho,\zeta)z \tag{6}$$

at a distance z downstream. Note as the beam drifts that the ratio of the beam divergence to the radius becomes a function of ρ and ζ, the position within the bunch. The bunch emittance grows as a result of this spread in the ratio. Let us assume that there is a lens at a position $z = z_l$ with a focal length of

$$f = \frac{z_d^2}{2(z_l + z_d)} \,. \tag{7}$$

Then, at a position z_d further downstream from the lens, the ratio of the beam divergence to the radius is

$$\frac{r'(\rho,\zeta)}{r(\rho,\zeta)} = \frac{2(z_l + z_d)}{z_d(z_d + 2z_l)} \tag{8}$$

which is independent of the particle's position within the bunch. Thus the effect of the lens has been to rotate the lines in phase space corresponding to different axial slices onto each other, therefore eliminating the emittance growth.

For this model, the normalized emittance can be rewritten as a function of the axial position and lens focal length as

$$\varepsilon_{x,n} = \frac{1}{2}\beta\gamma\sqrt{\langle\Lambda^2\rangle\langle\rho^2\rangle - \langle\Lambda\rho\rangle^2}\left(2r_o(z_l + z_d) - \frac{z_d^2 r_o}{f}\right) , \tag{9}$$

which explicitly shows that the emittance can vanish for arbitrary lens positions and drift distances, with the proper choice of lens focal length. The quadratic cancellation leads to good compensation over a broad minimum as the beam drifts followed by a rapid nonlinear increase in the emittance.

It is worth noting that the cancellation occurs both with radial or axial nonlinearities. Also note that after compensation the ratio of r' to r is the same for all slices but r' and r are not.

The physics in a photoinjector is much more complicated than in this model, but much of the same happens in the next subsection as we include an axial variation in the force.

2.2 *Analytic Model Using Linear Expansion of Fields*

In this section, we will no longer assume that the force is independent of the position along the beam line, z. However, we will assume that the forces are radially linear for the time being. The physics discussed in this section will represent the dominant physics if the beam is long and we will see that the compensation scheme only leads to cancellation of the emittance growth which originates from the constant and linear terms in an axial Taylor

series expansion of the radial space-charge forces. In general we can write the radial position and divergence for a particle as

$$\frac{r(\rho,\zeta,z)}{\rho} = r_o + \int_0^z \int_0^{z'} \hat{\Lambda}(\zeta,z'')dz''dz'' \tag{10}$$

and

$$\frac{r'(\rho,\zeta,z)}{\rho} = \int_0^z \hat{\Lambda}(\zeta,z')dz' \tag{11}$$

before the lens where the forces are given at the radial beam edges and $\hat{\Lambda}(\zeta,z) = \Lambda(\rho,\zeta,z)/\rho$. The particle positions and divergences are

$$\frac{r(\rho,\zeta,z_l+z_d)}{\rho} = r_o\left(1-\frac{z_d}{f}\right) + \int_0^{z_l+z_d}\int_0^{z'} \hat{\Lambda}(\zeta,z'')dz''dz' - \frac{z_d}{f}\int_0^{z_l}\int_0^{z'} \hat{\Lambda}(\zeta,z'')dz''dz' \tag{12}$$

and

$$\frac{r'(\rho,\zeta,z_l+z_d)}{\rho} = \int_0^{z_l+z_d} \hat{\Lambda}(\zeta,z'')dz''dz' - \frac{1}{f}\int_0^{z_l}\int_0^{z'} \hat{\Lambda}(\zeta,z'')dz''dz' - \frac{r_o}{f} \tag{13}$$

after a drift z_d past the lens at $z = z_l$. In order to find something useful out of Eqs. (12) and (13), lets expand the force about some axial location ζ_o,

$$\hat{\Lambda}(\zeta,z) = \hat{\Lambda}(\zeta_o,z) + \chi\hat{\Lambda}(\zeta_o,z) + \chi^2\hat{\Lambda}''(\zeta_o,z) + \ldots \tag{14}$$

where we have defined $\chi = \zeta - \zeta_o$ and the derivatives are with respect to ζ.

If we just keep the first order expansion terms, the particle's radius and divergence are given by

$$\frac{r(\rho,\zeta)}{\rho} = \chi\left(a_1 - b_1\frac{z_d}{f}\right) + (a_o + r_o) - (r_o + b_o)\frac{z_d}{f} \tag{15}$$

and

$$\frac{r'(\rho,\zeta)}{\rho} = \chi\left(c_1 - b_1\frac{1}{f}\right) + c_o - (r_o + b_o)\frac{1}{f} \tag{16}$$

where the coefficients a_i, b_i, and c_i are given by

$$a_i = \int_0^{z_l+z_d} \int_0^{z'} \hat{\Lambda}^{(i)}(\zeta_o, z'')dz''da' \tag{17}$$

$$b_i = \int_0^{z_l} \int_0^{z'} \hat{\Lambda}^{(i)}(\zeta_o, z'')dz''dz' \tag{18}$$

and

$$c_i = \int_0^{z_l+z_d} \hat{\Lambda}^{(i)}(\zeta_o, z')dz' \,. \tag{19}$$

The normalized force can be redefined to include axial acceleration, if required, without requiring modification of the form of these equations.[13] Requiring the ratio r'/r to be independent of χ is equivalent to requiring

$$r' \frac{dr}{d\chi} = r \frac{dr'}{d\chi} \,. \tag{20}$$

Using Eqs. (15) and (16) to solve Eq. (20) we find that the terms with χ and the terms quadratic in $1/f$ each cancel exactly, and we are left with

$$0 = a_1 c_o - c_1(a_o - r_o) + \frac{1}{f}(-c_o b_1 z_d - a_1(b_o + r_o) + b_1(a_o + r_o) + c_1 z_d(r_o + b_0)) \tag{21}$$

which can be used to solve for the focal length in terms of the integrals of the normalized force for the reference axial position. Thus, if a beam's space-charge force can be represented by just the constant and the linear expansion terms in Eq. (14) we expect complete emittance compensation if a positive solution exists for the lens' focal length (Eq. (21)) (a negative solution will defocus the beam).

There are some interesting consequences to this model. First, there is not always a physical solution for the focal length. Note that the constant term in Eq. (21) does not vanish as z_d does, but the linear (in $1/f$) terms does (note the definitions of the coefficients in Eqs. (17)–(19) — the a_i's approach the b_i's as z_d becomes zero). Thus the solution for the focal length diverges as z_d vanishes and after some sufficiently short z_d compensation is impractical. Next, note that any nonlinear axial or radial contribution to the force will not cancel. Thus we can only expect to make this compensation work over an axial section of the beam where the radial space-charge force is represented well by a linear axial expansion. If the beam becomes non laminar the higher-order terms in Eq. (14) are no longer small and the maximum axial length that can be compensated over can become very short. We can use the nature of Eq. (14) to predict what we would expect the compensated beam's phase space to look like. Over the region that the higher order contributions are small we expect to see all the particles line up in phase space. As we move away from the axial location

of compensation, ζ_o, χ becomes bigger and the quadratic term (or higher order terms) will become important, and we expect that the particles from these locations will fan further and further away from the dominant line, until the end of the bunch is reached. This is similar to what we see in Fig. 1.

Now consider the case when the beam is being focused to a beam-radius minimum. If the space-charge forces are sufficiently weak, all particles will cross through the beam's center; e.g. a particle starting at a negative x position will end up with a positive x value. We can describe this focusing behavior as a beam *crossover*. On the other hand, if the space-charge forces are very strong, the particles will be reflected away from the beam center and the horizontal and vertical positions of a particle will not change sign. This behavior can be described as a beam *waist*. As a beam is focused, the part of the bunch with current above some critical value will create a waist and the part with current below that value will form a crossover. Most electron bunch current profiles have a high current center surrounded by low current tails. Often, the particles at the ends of the bunch will crossover while the particles at the center of the bunch will form a waist. Under this condition the beam's phase space will bifurcate; there exists particles that were initially infinitesimally close in phase space that end up a finite distance apart. This phenomena has also been seen for intense DC electron beams (although the bifurcation appears radially instead of along the longitudinal position within the bunch).[14] Virtually all beams have at least partial bifurcation during focusing. One of the most important design criteria for photoinjectors is to minimize the amount of the beam actually crossing over. In practical designs, less than one per-cent of the total bunch charge crosses over, and the bifurcation can be ignored. If a substantial amount of the bunch crosses over, the linear axial space-charge field approximation is useless for the bifurcated part of the beam, and only the non bifurcated part can be compensated. Note also that if the whole beam crosses through the beam's center, the crossover will occur at different axial positions along the beam line for different longitudinal slices along the bunch, preventing any significant amount of compensation.

In principle, we could explicitly calculate the emittance for an actual photoinjector by including the nonlinear terms in Eq. (14) in an analysis and by numerically calculating the coefficients a_i, b_i and c_i. Unfortunately, this is not practical because of the required complexity. Instead, we will use a simpler numerical model, which we will present in Section 3 to generate quantitative results. The main conclusions from this section is that (1) the residual emittance is minimized if the beam laminarity is maximized and (2) there is only cancellation of the linear expansion over a limited range of lens locations.

For the rest of this section, we describe qualitatively the real physics. We show that the physics in the short-beam regime can be represented by the first model and the physics in the long-beam regime can be represented by the second model. Thus, the essential physics for determining the residual space-charge induced emittance after compensation is contained in the long-beam limit for typical bunch charges (because the emittance growth due to the first model will vanish). In Section 3 we give normalized quantitative results in the long-beam limit, which then lead to universal compensation curves.

2.3 Actual Photoinjector Physics

In this subsection we relate the actual physics in a photoinjector to the models in the previous subsections. We argue that the residual emittance is dominated by the nonlinear terms in the

axial Taylor expansion while the beam is in the long-bunch regime and that the contribution while the beam is short is negligible. We also present a numerical simulation using an accelerator design code and verify our argument by examining the predicted phase-space plots. Once we have established that, we are confident that we are able to numerically calculate the residual emittances using the model in Section 3.

Thermionic injectors can produce extremely low-emittance electron bunches, although with low charge and current.[15] Photoinjectors are used for applications requiring the combination of high-peak current and low emittance. There are two ways to achieve high current in a photoinjector.[16] First, the electron bunch can be initiated very long and then bunched with dispersive magnetic elements. Alternatively, the bunch can be made as small as possible from the beginning with later magnetic bunching if required. Although the emittance compensation scheme works similarly in both situations, the first case has larger emittance growth from the rf fields (check Eq. (2)), and the shortest possible initial bunch is usually chosen. For bunch charges (1–10nC) and gradients (10–100MV/m) of typical interest, a short bunch initially looks like a thin pancake as it leaves the cathode but transforms into a long cylinder in its own frame of reference as it is accelerated. Assume the bunch has uniform radial-charge density. In the first regime, the radial space-charge force is radially nonlinear but the same for all axial positions. In the latter regime, the space-charge force is radially linear but varies in magnitude with the axial position within the bunch. This is true independent of the axial-charge distribution as long as the rms bunch length (at the moment the bunch leaves the cathode) is short in comparison to the rms radius. Using non relativistic kinematics, we find for example that a 1 ps long bunch in a 100 MV/m field has $< 10\ \mu$m physical length as it leaves the cathode. For a uniform density slug, this force can be empirically represented by[13]

$$\Lambda(\rho,\zeta) = \rho\frac{\Lambda_o}{\gamma^2\beta^2c^2}\left(1 + 2.25\rho^2 e^{-A_r/0.85} - \frac{\zeta^2}{2}\left(1 - e^{-A_r/0.36}\right)\right), \tag{22}$$

where the normalized force is

$$\Lambda_o = \frac{eQ}{2m_o\varepsilon_o\pi r_o\sqrt{(\beta c\tau_b)^2 + 4r_o^2}}, \tag{23}$$

τ_b is the bunch length in time, Q is the bunch charge, and A_r is the beam's aspect ratio (length divided by radius) in its own frame of reference,

$$A_r = \frac{\gamma\beta c\tau_b}{r_o}. \tag{24}$$

The nonlinear behavior in the short-beam (pancake) limit is counter intuitive. First, the radial force has no axial dependence, if the beam is sufficiently short. Also, the radial space-charge force diverges at the beam edge for short beams (Fig. 3). This can be seen by explicit calculation of the radial electric field from a slug beam of radius a and length L,[5]

$$E_r(r,z) = 4\sqrt{\frac{a}{r}}\int_0^L \rho_o[K(X)(1/X - X/2) - E(X)/X]dz' \tag{25}$$

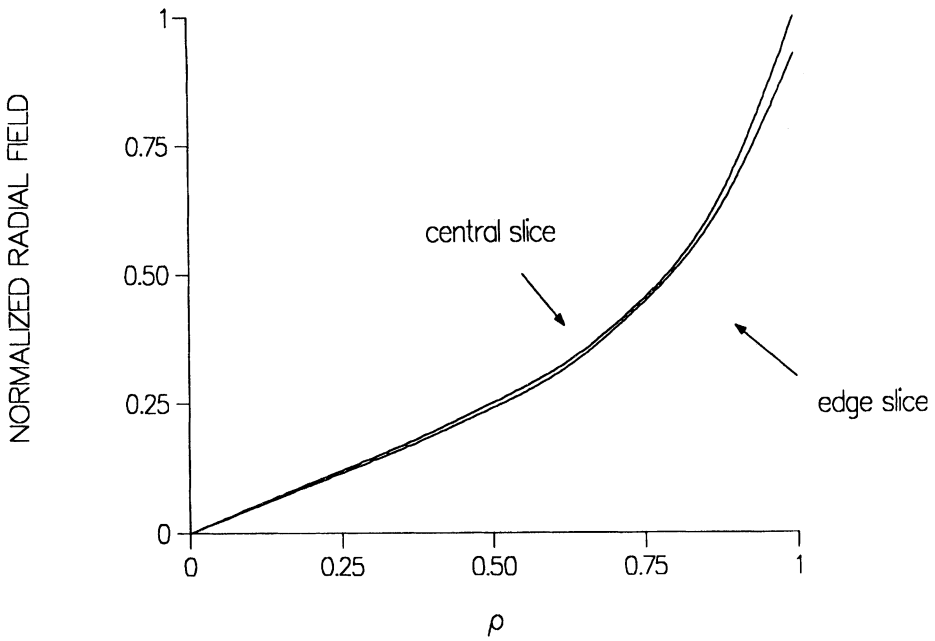

FIGURE 3: Radial electric field versus radius in the short beam limit (aspect ratio 0.1) for both the center and an edge slice.

where the radial and azimuthal integration has already been done, ρ_o is the charge density, K and E are the complete elliptical integrals of the first and second kind, respectively, and

$$X = \sqrt{\frac{4ar}{(z-z')^2 + (a+r)^2}}\,. \tag{26}$$

Note that the $(z - z')^2$ term is small compared to the second term in the denominator in this regime and that the elliptical integrals diverge as the bunch length vanishes and X approaches one, resulting in the nonlinear radial forces.

This effect can be physically understood by comparing the pancake-of-charge to a homogeneously filled ellipsoid. There is no emittance growth if the bunch is purely ellipsoidal. The potential for a homogeneous ellipsoid-of-charge defined by

$$\frac{r^2}{a^2} + \frac{z^2}{c^2} = 1 \tag{27}$$

is given after direct integration (see for example[17]) by

$$V(r,z) = k\left\{\left(\frac{\pi}{2} - \tan^{-1}\frac{c}{\sqrt{a^2-c^2}}\right)\left(\frac{2}{(a^2-c^2)} + \frac{2z^2}{(a^2-c^2)^{3/2}} - \frac{r^2}{(a^2-c^2)^{3/2}}\right)\right.$$
$$\left. - \frac{2z^2}{(a^2-c^2)c} + \frac{cr^2}{(a^2-c^2)a^2}\right\} \tag{28}$$

for thin ($c < a$) distributions, where k is a constant related to the ellipsoid charge density. Both the radial and axial forces are linear and independent of the other variable, leading to no emittance growth. Thus, this ellipsoid will expand to another ellipsoid (however, since the ratio of radial to axial forces is

$$\frac{F_r}{F_z} = \frac{r}{z}\frac{-\left(\frac{\pi}{2} - \tan^{-1}\frac{c}{\sqrt{a^2-c^2}}\right)(a^2-c^2)^{-1/2} + \frac{c}{a^2}}{2\left(\frac{\pi}{2} - \tan^{-1}\frac{c}{\sqrt{a^2-c^2}}\right)(a^2-c^2)^{-1/2} - \frac{2}{c}}, \tag{29}$$

the ellipsoid will not expand to a self-similar shape). An infinitesimally thin ellipsoid-of-charge (which has linear radial-space-charge forces) has an axially integrated radial charge density of

$$\rho(r) = \rho_o\sqrt{1 - \frac{r^2}{a^2}}, \tag{30}$$

which is not the same as a uniformly filled pancake-of-charge. The drive laser could be designed to form this radial charge density, which would eliminate the emittance growth near the cathode. However, such a design would increase the emittance growth in the long-bunch regime, which we will see is the dominate emittance growth mechanism, and in general is not advisable.

Thus we expect that the emittance growth in a photoinjector is dominated by radial nonlinearities in the short-bunch regime and axial nonlinearities in the long-bunch regime. If we use an external solenoid around the photoinjector for the linear force required for the compensation, it can be argued that this emittance compensation can be tailored to work for both the radial and axial nonlinearities (originally in Reference 13, but reproduced in the Appendix for convenience), even though they occur at different times within the bunch's existence. This is because various accelerator parameters (like phasing, average gradient, rf cavity design, etc.) will effect how quickly the radial nonlinearities are replaced by the axial nonlinearities and because the focusing force is axially distributed. If we have complete flexibility in defining the field profile from the external soleniod, we then have the ability to provide different effective thin-lens strengths and effective thin-lens placements for the compensation of the radially nonlinear forces and of the axially nonlinear forces. A 10 ps long, 4 mm radius bunch has an aspect ratio of unity after only 250 KeV of acceleration. After this point the beam can be considered in the long-bunch regime. In typical photoinjectors, there is little radial expansion over this short distance, and the crude model in subsection *A* can be expected to demonstrate the essential physics in the short-bunch regime. Recall in that

model the compensation left no residual emittance growth, independent of the lens position; thus we expect negligible residual emittance growth from the forces within the short-bunch regime even if the effective thin-lens placement is optimized for the axially nonlinear forces (since we have independent control of the effective thin-lens strengths for the two regimes). Let us then assume that the design has maximum compensation for emittance growth in both the short- and long-bunch regimes. We expect that the residual emittance is dominated by the nonlinear forces from the long-bunch regime and we can estimate the residual emittance by only considering the effects from the long-bunch regime. In order to verify this argument we can examine plots of the particles' phase-space distribution after compensation.

The design studies for a 5 nC, 26 MV/m photoinjector using the particle-pushing code PARMELA[18] have shown that a 10 ps initial pulse length leads to the minimum final bunch length.[19] As the bunch becomes shorter, the axial space-charge force increases, resulting in a longer final bunch length. Using a Gaussian longitudinal distribution with a 10 ps FWHM and an external solenoid for compensation we achieved the final phase-space distribution shown in Fig. 4(a), at 20 MeV. The normalized slice emittance is only 1 π mm mrad, and the axially integrated rms emittance is 5 π mm mrad. The normalized rms horizontal emittance is shown in Fig. 4(b) as a function of position along the beam line. In this figure, the monotonic reduction of the normalized emittance is clear, and the final normalized emittance is roughly 1/5 of the maximum normalized emittance, occurring near the cathode. A solenoid around the first few accelerating cells provides the focusing for the compensation. While the beam is in the axial magnetic field from this solenoid, the conservation of the canonical angular momentum results in an emittance growth which then vanishes as the beam exits this field. In order to show the compensation clearly (and to prevent speculation that the emittance growth and reduction might simply be the result of the beam entering and leaving a region with axial magnetic field) the effect of the canonical angular momentum introduced by the focusing magnetic field has been subtracted out from the normalized emittance shown in Fig. 4(b). Any residual emittance from the short-bunch regime would be manifested as a curvature in the phase-space distribution. The final phase-space distribution is dominated by a bow tie shape, with only some small curvature along the bow tie's edges; thus the final emittance is not influenced significantly by the initial emittance growth in the radially nonlinear regime. This conclusion can also be made by noting that the slice emittance is just one fifth of the rms emittance. We see that for this class of high-charge photoinjectors we would only need to estimate the residual emittance resulting from the emittance growth in the long-bunch regime. The bow-tie thickness is dominated by particles at the axial edges of the beam. These particles strongly influence the final emittance even though they often carry little charge. The bow-tie shape is caused by the failure of the linear axial-field approximation (Eq. (14)). The further away a particle is from the nominal compensation location ζ_o, the larger the nonlinear forces are (which cannot be compensated). The large nonlinear forces lead to a scatter in the particles' phase-space distribution, generating the bow-tie shape and the residual emittance. Particles which bifurcate in phase-space will not appear in the main bow-tie, but will show up as a spur to the main distribution often with their own bow-tie figure. There is some slight indication of this effect in Fig. 4(a) near the $x' = 0$ axis. Unfortunately, the amount of bifurcation and the spread in the bow-tie is hard to predict analytically. It is these effects we plan to numerically investigate in the next two sections.

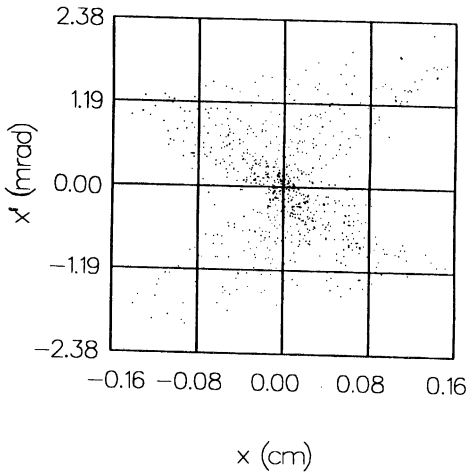

(a)

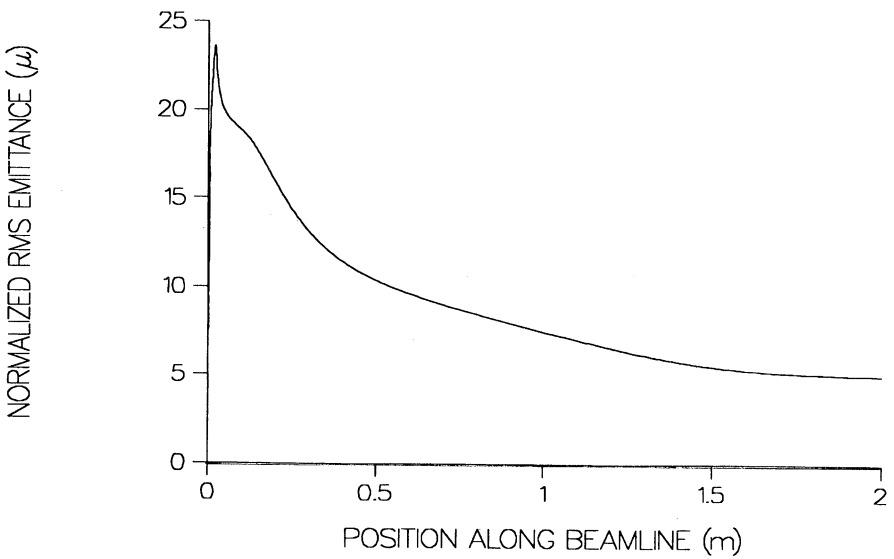

(b)

FIGURE 4: (a) Final phase-space distribution for an actual photoinjector at 20 MeV. (b) Normalized rms emittance as a function of position along the beam line. The photocathode is located at the origin and the accelerator tank is roughly 1.2 m long.

Finally, consider a photoinjector with the lens too far from the cathode to provide any compensation in the short-bunch regime. (This can result from having too high a gradient.) In this special case we would expect that the residual emittance to be dominated by radial nonlinearities, and that the slice emittance to be equal to the axially integrated rms emittance. The emittance in this case might be improved by using a transverse laser-intensity profile of the form given in Eq. (30). There would be no short-bunch-regime emittance growth at all in this case (because the radial space-charge fields would be linear), but we would again expect a larger emittance growth in the long-bunch regime from the new radial nonlinearities. Although we do not expect good compensation for these radial nonlinearities (from the linear expansion model), the final emittance may still be smaller, depending on bunch aspect ratio and gradient.

Now that we are confident that we can estimate the residual emittance by only including the physics found in the long-bunch regime, we will introduce a simple numerical model for the long-bunch regime in Section 3. We will use this numerical model to generate universal curves for the residual emittance from the long-bunch nonlinearities. Note first that (1) a bucking coil must be placed behind the cathode to eliminate the axial magnetic field at the cathode (which will contribute to the emittance); (2) because the external solenoid takes up physical space outside the accelerator cells and the presence of the bucking coil, the effective lens center cannot be arbitrarily close to the cathode; (3) rf focusing (deformation of the cavity back wall to introduce radial electric rf fields (Fig. 5)) can be used to move the

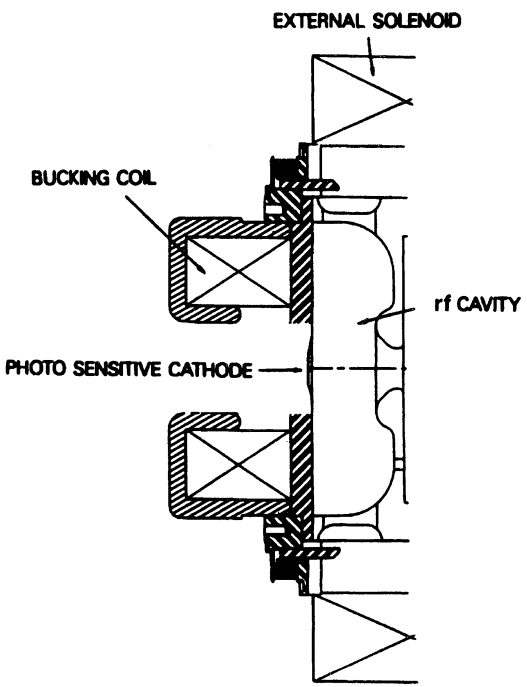

FIGURE 5: Detail of the first cavity in the APEX photoinjector, showing geometry introducing rf focusing.

effective lens position upstream but at the cost of large rf-induced emittance growth (both slice and rms);[20] and (4) the longitudinal beam shape tends to become parabolic even if it starts from a Gaussian distribution.[19,20] A good approximation to use in the long-bunch limit is a triangular current distribution along the bunch with a uniform radial distribution. Recall that the emittance growth from a triangular distribution is only 10% larger than that from a parabolic distribution and about one-half that from a Gaussian distribution from Eq. (3).

3 NUMERICAL MODEL IN LONG-BEAM REGIME

In this section we present the numerical model to calculate normalized emittance curves (before and after compensation) in Section 4. The purpose of this section is to establish a tool that we are confident will predict the residual emittance and which we can use to determine scaling behavior. The numerical model must include the long-bunch-regime physics and the effect from a focusing lens. We also show that the model is consistent with the space-charge model used in previous uncompensated emittance estimates.[4] This model will just investigate the emittances induced from the space-charge forces and thus the accelerating field gradient is important but the actual rf frequency is not. In order to predict the complete emittance growth for a given photoinjector design, the rf emittance (Eq. (2)) should be added in quadrature to the residual emittance calculated from this model.

We start with the radial and axial force equations,

$$\frac{d}{dt}\gamma m_o \dot{r} = \frac{eE_r}{\gamma^2} \tag{31}$$

and

$$\frac{d}{dt}\gamma m_o \dot{z} = eE_z \, . \tag{32}$$

We will make the following assumptions:

(1) The radial force is from the space charge only (including the self-magnetic field).

(2) The axial force is from a uniform, DC field E_z only.

Assumptions (1) and (2) are critical to the numerical model used in the next section. This model fails for cases in which the emittance growth from the time-varying rf field is larger than the uncompensated space-charge induced emittance growth (because of the large transverse focusing shear across the beam). If it is not, though, the effect of the radial rf forces is to modify slightly the effective lens position and strength.[1] This is not an important limitation because the actual focusing in a photoinjector is not done by an infinitely thin lens anyway and the normalized data we present in the next section are meant to indicate residual emittances possible for given gradients and beam parameters as opposed to give precise design information for the focusing. The effect of having a sinusoidal axial field instead of a DC field again just slightly modifies the lens positions and strength because of the fields' influence on the beam's proper time (see[13] or the Appendix).

(3) The radial force is linear with the radius, so we need only to calculate the equation of motion at the radial edge of a bunch slice. This requires a uniform transverse charge density.

(4) The current profile is triangular in time. We calculate the emittance by using the rms radius and divergence values for several slices along this current profile.

(5) The radial motion is non relativistic; thus we can write

$$\gamma = \frac{eE_z}{m_o c^2} z + 1 \,. \tag{33}$$

(6) We can define a normalized radial electric field parameter η to be

$$\eta = \frac{rE_r}{r_o E_z} \,, \tag{34}$$

where as before r_o is the initial beam radius. Note that the edge peak radial electric field using Gauss' law in the long-bunch approximation is

$$E_{r,\text{peak}} = \frac{I_{\text{peak}}}{2\pi\varepsilon_o \beta c r} \,, \tag{35}$$

so the peak η along the triangular current profile is proportional to the peak current. Thus the peak η can be thought of as a normalized peak current, and we will use it in this manner later. Note that $rE_{r,\text{peak}}$ is inversely proportional to β and diverges as the beam velocity vanishes (such as near the cathode). However, for the numerical integration we will assume for any given slice of the beam that η is a constant for the numerical integration, defined with $\beta = 1$ in Eqs. (34) and (35). This brings up the question of this model's validity near the cathode. In fact, direct integration of Eq. (31) yields a divergence in the beam emittance using Eq. (35) if the beam is initially at rest. We can justify the approximation in Eq. (34) by physical reasons because (a) the beam is not experiencing the long-bunch nonlinearities we wish to study while β is significantly less than 1, (b) the Gauss' law approximation is invalid for a short bunch length, and (c) the cathode is on a metal surface that shorts out the radial electric field initially. This approximation is also made in other analytic treatments (e.g., Eq. (40) in Reference 4). Note that the radial electric field at a point $r < r_o$ is from a higher average charge density than the field at the edge because the beam is being accelerated. This introduces an additional nonlinearity in the short-bunch regime that somewhat compensates for the effect seen in Fig. 3.

(7) Although we can directly integrate Eq. (31) to find the radial velocity as a function of radius, we lose the axial dependence on these variables that is needed for an emittance calculation at a given point. As a result we numerically integrate Eqs. (31) and (32) using

$$\Delta\dot{r} = \left(\frac{a\eta c^2 r_o}{\gamma^3 r} - \frac{a\dot{z}\dot{r}}{\gamma} \right) \Delta t \tag{36}$$

and

$$\Delta\dot{z} = \frac{ac^2}{\gamma^3}\Delta t \tag{37}$$

where a is the normalized axial acceleration

$$a = \frac{eE_z}{m_o c^2}\,, \tag{38}$$

and the time step Δt is kept constant in the bunch's frame of reference. Note that η is not a function of the beam slice radius and that this model allows the beam to expand and contract arbitrarily.

(8) We will use an initial cathode area of 1 cm^2 and a constant accelerating gradient of 10 MV/m and scale the results with the formulae provided in Section 4. A beam current of 531 A corresponds to $\eta = 1$. We will calculate the emittance after acceleration to a sufficiently high energy (100 MeV) so that it will remain constant thereafter unless there are extremely long drifts (see Eq. (3)). We will use a time step of 10 fs.

(9) We assume that an infinitesimally thin linear lens exists at the axial position z_l, with focal length f, that modifies a particle's divergence by

$$\Delta r' = \frac{r}{f}\,. \tag{39}$$

As the lens focuses the bunch slice, the radial force increases (Eq. (35)). If the slice is focused too small, the divergence in the radial force introduces noise in the calculation. The noise could be addressed by decreasing the time-step size further, or, more simply, by introducing a small slice emittance, which allows the slice edge to cross the axis (from a positive x to a negative x) rather than reflect back to positive x. This is done by making the radial force linear within a radius defined by

$$r_{\text{emit}} = \frac{\varepsilon_{\text{slice}}}{ar_l}\log\left(\frac{\gamma + \sqrt{\gamma^2 - 1}}{\gamma_l + \sqrt{\gamma_l^2 - 1}}\right)\,, \tag{40}$$

where r_l is the slice size at the lens and γ_l is the slice's relativistic factor at the lens. We use a slice emittance $< 1\pi$ mm mrad for the simulations in Section 4.

4 SIMULATIONS OF RESIDUAL EMITTANCE AFTER COMPENSATION

In this section, we present the results of the residual emittance calculations. The goal of this section is to be able to predict the residual emittance for any short-pulse photoinjector design. This means we wish to be able to predict the residual emittance as a function of cathode radius, peak current, and accelerating gradient, but not necessarily as a function of precise lens position and strength (as was discussed earlier). In fact, most photoinjector designs using this compensation technique are meant to be operated over some range of

beam parameters (charge, current, and so on) and as a result the focusing scheme is designed to be flexible[7,8] so precise lens information is not essential.

Providing the residual emittance data as a function of all three variables would be overwhelming. However, we can easily reduce the amount of required data by presenting normalized residual emittance calculations and a set of scaling laws that allows us to map the provided curves to any combination of cathode radius, current and accelerating gradient. Each simulation then becomes a family of simulations corresponding to different currents, accelerating gradients, and emittances. This section is the major thrust of this paper. From the results we expect to be able to predict compensation performance and the residual emittance for any short-pulse photoinjector design and determine scalings which lead to better compensation and lower residual emittances. Comparison with actual emittance measurements will be made in the next section.

We calculate the emittance for an uncompensated bunch with a triangular current profile as a function of the peak normalized current, η for a DC accelerating gradient. We find counter intuitive physics around a peak η of 1 and plot the emittance versus lens position (optimizing lens strength) for that value. We learn that there are two distinct focusing methods to use for compensation. We plot the residual emittance versus peak η for a fixed lens position, and finally we plot the residual emittance versus the accelerating gradient for a typical cathode-to-lens spacing. If physical constraints are present on the effective lens position, a minimum emittance exists at moderate gradients. Qualitative agreement with the model in subsection 2.2 will be noted whenever possible as a check on this method.

4.1 Normalization Rules

In this section, we find normalization rules which allow us to scale the residual emittance calculations from normalized simulations to any accelerating gradient, cathode radius and current. There are many sets of normalization rules possible. We will pick the simplest one that is consistent with the approximations in the previous section.

First, let's assume we know the emittance growth for a specific case. Because the radial space-charge force is linear, the ratio of dr/dz to r is the same for any radial position in a single slice at any given axial position. If we take any radial core of this beam, the emittance will be the original beam's emittance times the ratio of the radii squared. Likewise, the current in the core is the total current times the same ratio squared. Thus, the emittance and the current scale with the cathode area for a given accelerating gradient, axial current density distribution and a set of focusing parameters.

Next, we need to find a scaling law that lets us transform the accelerating gradient. We will find this scaling by examination of Maxwell's equations. Consider a charge Q passing through an rf cavity of characteristic frequency f. We can assume the energy gain of the charge from the cavity fields and space charge are independent of f. Because the length scales inversely with f, the rf electric field must scale proportionally with the frequency and time must scale inversely with frequency. From the Maxwell equation,

$$\nabla \times \vec{B} = \vec{J} + \frac{\partial \vec{E}}{\partial t} \tag{41}$$

we additionally see that the magnetic field scales proportionally with the frequency and that the current density scales as the frequency squared. The current is independent of the frequency, and Q scales as the inverse of the frequency. Note that the beam emittance (normalized as well as unnormalized) scales as the inverse of the frequency.

Now, let's assume that the characteristic frequency f is extremely low and looks essentially DC to the beam. Say we now consider a second case with twice the gradient (by doubling f). The emittance for this case is 1/2 the emittance of the original case and the current density is 4 times larger.

With these rules, we can scale the residual emittance $\hat{\varepsilon}$ and the peak cathode current density from a simulation with a gradient of 10 MV/m, a cathode area of 1 cm^2, and a peak current of η to any arbitrary gradient and cathode area. Note that we have to retain the normalized peak current as an independent parameter. The current density scaled to a new gradient E_z is

$$J(E_z) = 531.\frac{A}{\text{cm}^2}\eta\left(\frac{E_z}{10\ MV/m}\right)^2 \tag{42}$$

and the cathode area scaled is

$$s = \left(\frac{10\ MV/m}{E_z}\right)^2 \text{cm}^2\ . \tag{43}$$

The normalized horizontal residual emittance for this area s and gradient E_z is

$$\varepsilon_{x,n}(E_z, s) = \hat{\varepsilon}\left(\frac{10\ \text{MV/m}}{E_z}\right)\ . \tag{44}$$

For a cathode area of S, the beam current is

$$I(E_z, S) = 531.\frac{\text{A}}{\text{cm}^2}\eta S\left(\frac{E_z}{10\ \text{MV/m}}\right)^2 \tag{45}$$

and the emittance is

$$\varepsilon_{x,n}(E_z, S) = \varepsilon_{x,n}(E_z, s)\frac{S}{s} = \frac{E_z}{10\ \text{MV/m}}\hat{\varepsilon}\frac{S}{\text{cm}^2}\ . \tag{46}$$

The plan is to provide figures showing the normalized residual emittance $\hat{\varepsilon}$ as a function of normalized current η for a gradient of 10 MV/m and a cathode area of 1 cm^2. The emittance for any arbitrary accelerating gradient, cathode area and current can be found by this procedure: first, the appropriate normalized current η is found using Eq. (42). Then the normalized residual emittance $\hat{\varepsilon}$ is found from the figures using this η. Then Eq. (46) is used to find the residual emittance for the case with those particular parameters.

We can also define a lens position, $\hat{\varepsilon}$, normalized to the gradient by

$$\hat{z} = z_l\frac{eE_z}{m_o c^2}\ . \tag{47}$$

4.2 *Uncompensated Emittance*

In Fig. 6 we plot the uncompensated emittance for a triangular longitudinal distribution as a function of peak current η using the numerical model from the last section. We see two distinct regions, one above and one below a peak $\eta = 1$. For small current (peak $\eta < 0.1$), the effect of the space charge is to change the radial divergence but not the radius, leading to an emittance growth linear with current (which we see). For large current (peak $\eta > 100$), the initial beam size looks like a line source, and both the radius and radial divergences are changed. From Eqs. (31) and (35) we see that both the radius and divergence scale with the square root of the current, and the emittance should again scale linearly with the current (which we see). However, we see peculiar and counter intuitive behavior in the transition between these regimes near a peak $\eta = 1$, where the emittance actually decreases as the current increases. This appears to be in violation of Eq. (3). Recall, however, that Eq. (3) was derived assuming no appreciable beam expansion. We believe that the transition behavior results from some radial expansion that is similar to the original radial size, and which leads to a better homogeneous ellipsoid distribution than is present with slightly lower current.

4.3 *Residual Emittance Versus Lens Location*

In Fig. 7, we plot the minimum normalized emittance for a triangular longitudinal distribution with peak current $\eta = 1$ versus the normalized lens position while varying the lens strength. Note that the residual emittance for large lens positions ($\hat{z} > 4$) is the same as the uncompensated emittance. There are two distinct emittance minima, one at $\hat{z} = 0.85$ and the other at $\hat{z} < 0.2$. Examination of the slice trajectories shows that for the first minimum the beam is asymptotically focused to a waist as $\gamma \to \infty$, and the nonlinear space-charge forces after the lens compensate for the nonlinear space-charge forces before the lens. The location of the lens for the first minimum corresponds to the point at which the beam is about one fourth of the way to the end (corresponding to the retarded time in the beam's frame of reference). In the second minimum, the lens is very near the cathode and focuses the beam to a much earlier waist. The nonlinear space-charge forces after the waist compensate for the nonlinear space-charge forces before the waist. Significantly, there is only compensation if the lens position is relatively close to the cathode, and the best compensation is with the lens positions which lead to the most laminar beam flow, as predicted by the linear expansion model. The two minima merge to a broader minimum for either a peak $\eta > 3$ or a peak $\eta < 1/3$. In Fig. 8(a) we plot the ratio of dr/dz to r for the first minimum (at $\hat{z}$ near 0.85). Note that the particles with the same ratio of dr/dz to r will form a line in the beam's phase space. Particles from slices of the beam with normalized current densities in the range $0.75 \leq \eta \leq 0.8$ will pretty much lie along a single straight line in phase space, and not contribute to the residual emittance. Particles from nearby slices ($0.6 \leq \eta \leq 0.75$ and $0.8 \leq \eta \leq 1.0$) will end up near that line in phase space and particles from slices further away ($\eta < 0.6$) will scatter out further and further from that line in phase space. Thus the curve in Fig. 8(a) indicates good compensation around the peak of the current profile and that the residual emittance originates from the low-current tail as predicted in the model in subsection 2.2. Good compensation (defined by the minimum rms residual emittance) must have precisely these features. A scatter in

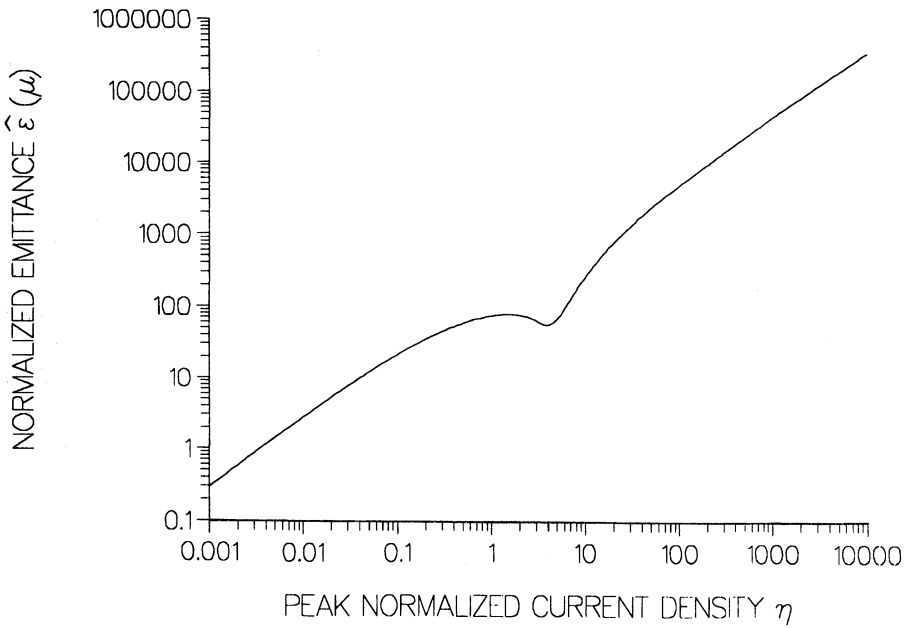

FIGURE 6: Uncompensated normalized emittance versus peak η.

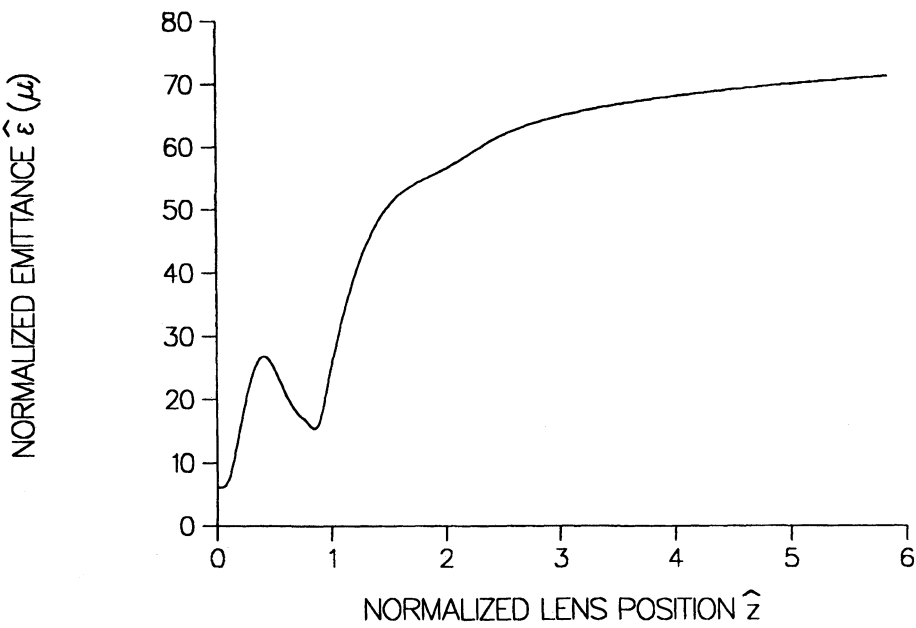

FIGURE 7: Compensated normalized emittance versus normalized lens position for peak η=1.

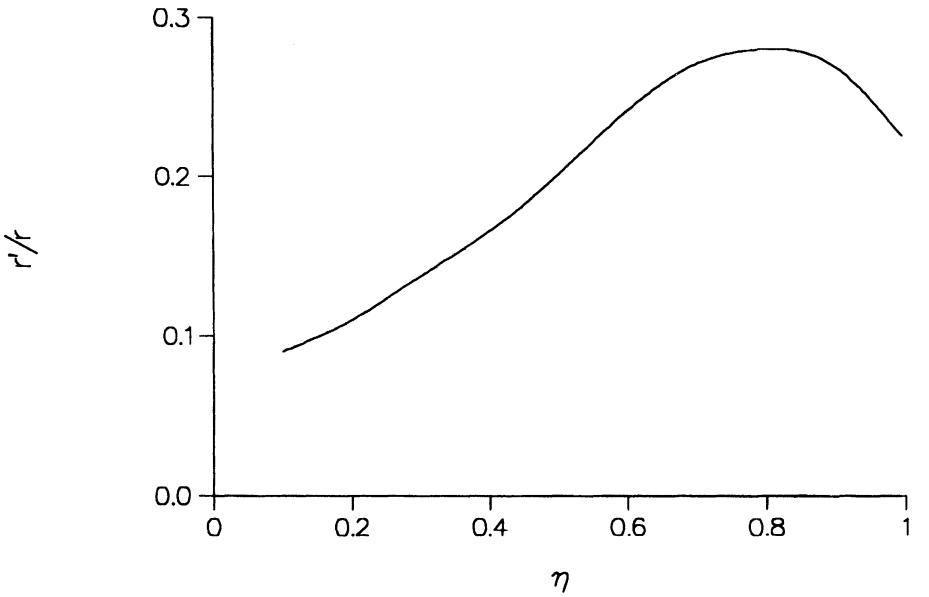

(a)

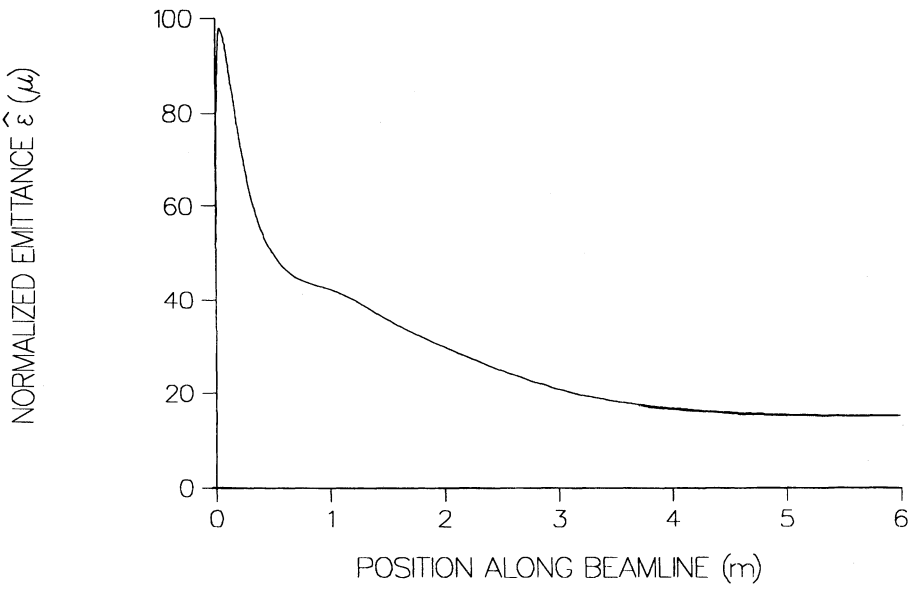

(b)

FIGURE 8: (a) Ratio of beam divergence to radius after compensation as a function of η within the bunch (b) Normalized rms emittance as a function of position along the beam line.

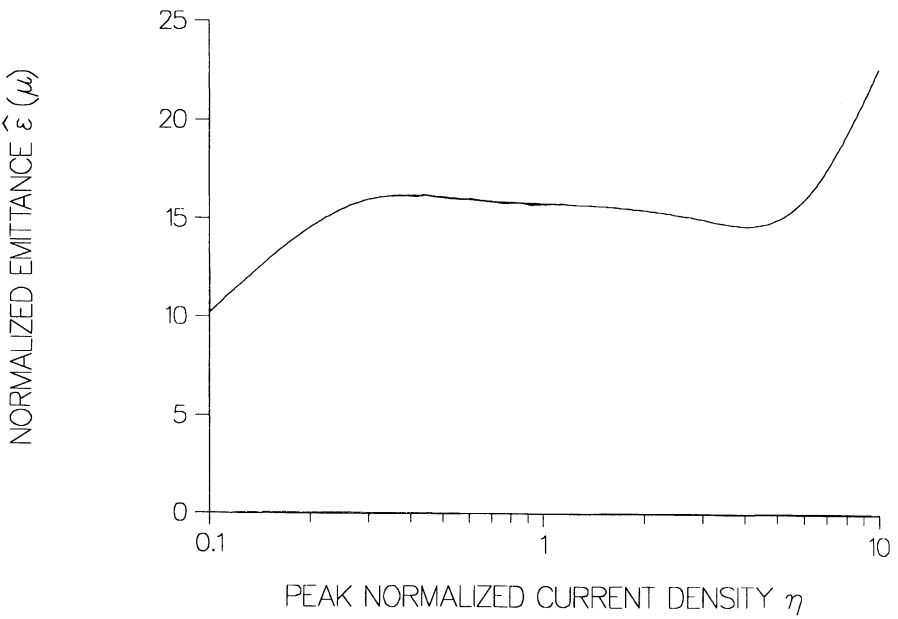

FIGURE 9: Compensated normalized emittance versus peak η.

the beam's phase space originating from particles in the bunch's low current tails influences the rms emittance much less than if the scatter originates from particles at the center of the bunch. Note also the absence of any bifurcation in Fig. 8(a) which would be seen as a discontinuity in r'/r. This implies that the beam crossover occurred for current densities $\eta < 0.1$ and will have little effect on the rms residual emittance. In Fig. 8(b) we plot the normalized rms emittance as a function of position along the "accelerator" beam line again for the first minimum. The effect of the emittance compensation is clearly demonstrated in this plot, and it shows both the initial emittance increase and the monotonic emittance decrease to an emittance minimum as required. Note that the emittance profile is similar to the one in Fig. 4(b) calculated by a detailed particle numerical simulation. The emittances in Fig. 8(b) are larger than those in Fig. 4(b) because the current is roughly five times larger. The ratio of the residual emittance to the maximum emittance in Fig. 8(b) is about half the size of the same ratio for Fig. 4(b) because the simulation used to calculate the emittances in Fig. 4(b) included all rf fields and thus the rf-induced emittance growth.

4.4 Residual Emittance Versus Peak η

In Fig. 9 we plot the residual emittance for a longitudinal distribution as a function of peak current η, optimizing both lens position and strength. As seen in the previous subsection,

the optimal lens position for any peak η corresponds to about one fourth of the time a bunch requires to travel down the beam line in its own frame of reference. We see that the emittance is flat between peak ηs of 1/3 and 3, as in Fig. 6. Fig. 9 is the universal curve we want. The residual emittance for any arbitrary design can be found by using this curve and the scaling procedure described after Eq. (46). Given a desired current and the operating gradient, the curve in Fig. 9 implies that we want a cathode size that corresponds to a peak η of about 3 for the minimum emittance. We can rewrite the emittance as a function of gradient and normalized current density (by using Eqs. (45) and (46)) as

$$\varepsilon_{x,n}(E_z, I, \eta) = \frac{10\text{MV/m}}{E_z} \frac{\hat{\varepsilon}(\eta)}{\eta} \frac{I}{531\text{ A}} , \tag{48}$$

where $\hat{\varepsilon}$ is found in Fig. 9 and η is the peak normalized current in the triangular-shaped bunch. Thus, if we can place the lens anywhere, the scaling in Eq. (48) immediately tells us that we want (a) to have as high a gradient as possible and (b) to operate near a peak η of 3.

4.4 *Emittance Versus Gradient For Practical Lens Positions*

Because of practical limitations (requirements from vacuum pumping and cooling), we are often unable to have complete freedom to position the lens. In principle, we can either use rf focusing at the cathode or place a small lens in the webbing between the first two rf cavities, but we introduce new problems. To eliminate rf emittance growth from radial rf-field nonlinearities, the boundary of the rf focusing must match the lowest-order space harmonic, satisfying this equation[3]

$$r^2 = w^2 - \left(\frac{4d}{\pi}\right)^2 \log\left(\sin\frac{\pi z}{2d}\right) , \tag{49}$$

where d is one-half the rf wavelength and w is a free parameter. Note that the cathode must be shaped like a horn which excludes the possibility of rf focusing. The field from a small lens in the web between the first and second cells is very sensitive to misalignments[20] and is subject to significant additional emittance growth.

In Fig. 10 we plot the ratio of normalized emittance $\hat{\varepsilon}$ to current versus gradient for a minimum lens position z_l of 4 cm. We see a dip in the normalized emittance at moderate gradients, which is smaller than emittances at higher gradients until we reach nearly 100 MV/m. The emittance decreases as the inverse of the gradient for low gradients, as predicted in Eq. (45). The rise in the emittance as the energy is increased starts at the point where the minimum lens position exceeds the position of the lens corresponding to the first minimum in Fig. 7. The first region (before the inflection) corresponds to a ratio of the normalized emittance to the peak η (see Eq. (45)) of about 2.3. The last region (after the inflection) corresponds to a ratio of the normalized emittance to the peak η of 14. The ratio of the normalized emittance to η transitions from 2.3 to 14 in the central region around the inflection. It must be emphasized that these are average accelerating gradients (with respect to the beam's frame of reference) with transit time factors and drifts included. High-gradient photoinjectors can be used in conjunction with long drifts to lower the average

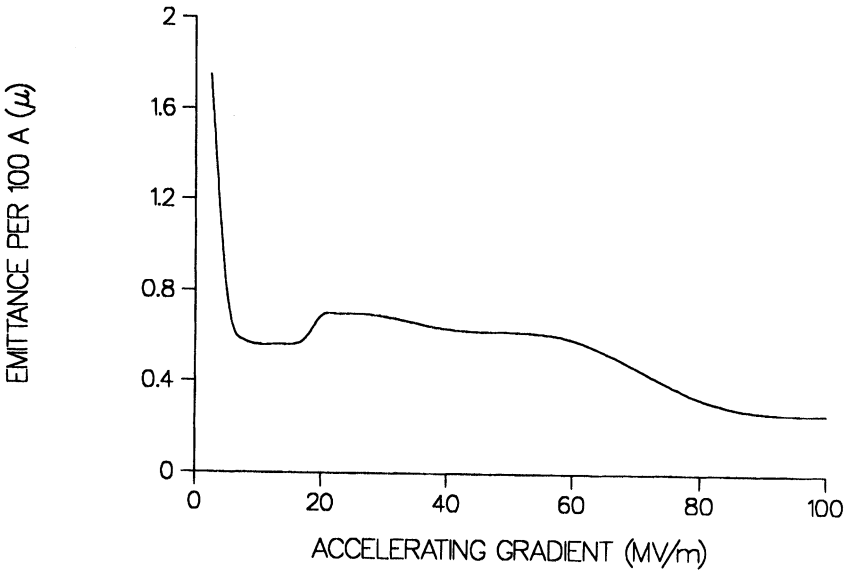

FIGURE 10: Compensated normalized emittance versus accelerating gradient for a cathode-to-lens spacing of 4 cm.

gradient enough to use the compensation scheme. However, we create a penalty in both rf emittance growth (Eq. (2)) and rf power requirements if we lower the average gradient significantly.

5 COMPARISON WITH EXPERIMENTAL EMITTANCE MEASUREMENTS

The compensation technique using an external solenoid around the first cell and a bucking coil behind the cathode has been verified experimentally and measurements have agreed well with particle simulations.[7,8,10] However, the emittances in the experiment and the simulations included effects from both the space-charge forces and the rf forces, which added in quadrature and were impossible to separate. In this section, we will compare the results from the previous section with the experimental results. Recall that the results from Section 4 did not include any effects from the rf fields and that we are actually trying to separate the two types of emittance growths. This is difficult to do, but a useful exercise because the rf-induced emittance growth can be drastically affected by rf cavity design, whereas the space-charge-induced emittance growth is only sensitive to average accelerating gradient and cathode size. The experimental results do not provide confirmation of the residual space-charge-induced emittance to better than about a factor of two because of the large rf-induced emittance growth in the experiment. However, the results in Section 4 are consistent with the measurements and this comparison provides some confidence in the normalized curves in Figs. 7, 9, and 10.

The 1.3 GHz photoinjector for the Los Alamos Advanced Prototype EXperiment (APEX) was the first photoinjector designed using the emittance compensation scheme. In Fig. 11 we plot the experimentally measurement emittance[21] and the uncompensated emittance from Kim's formula, for an average accelerating gradient of 10 MV/m. The experiment typically used a Gaussian transverse distribution clipped at the 36% intensity point. The experimentally measured emittance follows the empirical formula[22]

$$\varepsilon_{x,n} = 1 + e^{I/140}\pi \text{ mm mrad} \tag{50}$$

where the peak current I is in Amperes. The minimum emittance was found to be for a cathode radius of 3 mm at 130 A, 4 mm for 200–290 A, and 5 mm above 300 A and ranged from 3.5–12 π mm mrad. Kim's formula for the space-charge-induced emittance results in a normalized emittance of about 150 π mm mrad at 300 A, and his formula for the rf-induced emittance gives a normalized emittance of 0.03 π mm mrad. Kim's formulae clearly do not include the important physics associated with the APEX photoinjector.

After detailed analysis, we learned that the major emittance growth mechanisms were from the rf fields.[10] First, the rf focusing employed in the first cavity introduced strong radial electric fields. Also, the combination of the external solenoid and quadrupole symmetry of the coupling slots between cavities introduced an effective rotating quadrupole field. In Table 1 we summarize PARMELA simulations for 1 and 5 nC bunches. From Fig. 6 we see that the uncompensated emittance for a radially uniform 300 A bunch is about 70 π mm mrad, about one half that predicted from Kim's formula (which uses a Gaussian

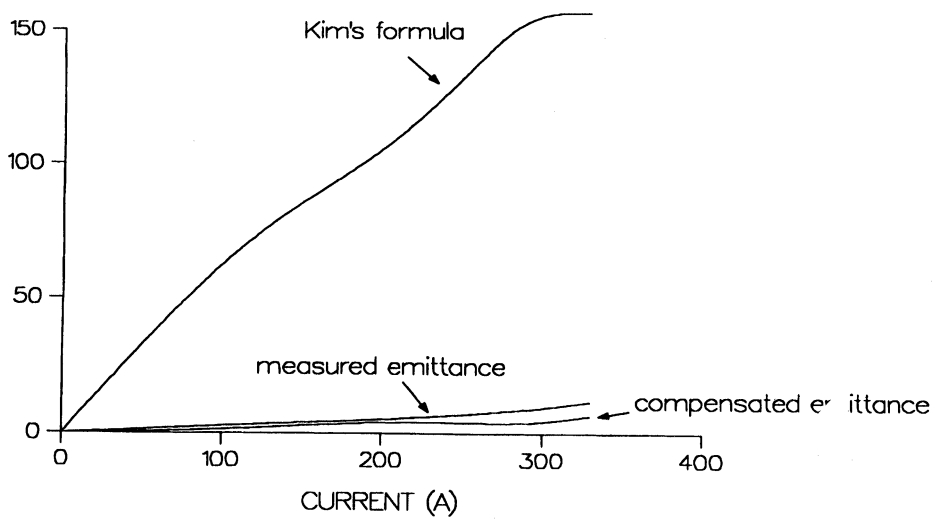

FIGURE 11: APEX measured emittance, Kim's emittance estimate, and compensated space-charge-induced emittance versus current.

radial profile). We see in Table 1 that there is only a small emittance variation (20%) between the compensated Gaussian current-profile and flat-top current-profile cases. This verifies the assertion that the precise axial current distribution is relatively unimportant.

The rf emittance growth from both the rf focusing and rotating quadrupole fields scales as the radius squared, plus higher order terms (compare with Eq. (2)). We expect that the overall emittance is the in-quadrature sum of the space-charge-induced emittance and the rf-induced emittance. Using the paraxial assumptions (3) and (5) in Section 3, it is clear that the radius at any axial point can be written as the cathode radius plus an axial function $f_1(z)$ times the cathode radius times the cathode current density. Now the instantaneous rf-induced emittance growth is another axial function $f_2(z)$ times the radius squared. The first axial function is essentially quadratic in z (because the radial acceleration is nearly constant) over the first cell (which contributes nearly all of the rf-induced emittance growth) and the second axial function typically is linear in z (from the lowest order expansion term from the sinusoidal rf field). After direct integration, we find that we can write the overall emittance as

$$\varepsilon_{x,n} = \sqrt{\varepsilon_{sc}^2 + c_1 \left(r_o + c_2 \frac{I}{r_o} \right)^4} \tag{51}$$

where we have ignored both the higher-order rf-induced emittance terms and the small correlation between the axial functions, and where ε_{sc} is the compensated space-charge-induced emittance and c_1 and c_2 are constants introduced by the rf focusing and the rotating quadrupole field. The constant c_1 is given by the axial integral of f_2 and the constant c_2 is given by the square root of the axial integral of $f_1^2 f_2$ divided by the square root of c_1. We can compare this form to the emittance fit in Eq. (50). Note that Eq. (50) is purely empirical, but the functional form of Eq. (51) is physical in origin and correct as long as the higher-order rf-induced emittance terms are small. We calculate c_1 by using Eq. (51) at zero current, and find $c_1 = 0.0123\ \text{m}^{-2}$. We can calculate c_2 by using Eqs. (50) and (51) at 330 A, and find $c_2 = 6.64\ 10^4\ \text{m}^2/\text{A}$. Using these values, we tabulate both the experimental emittances and the emittances from Eq. (51) for 130, 200, 250, and 290 A (corresponding to bunch charges of 1, 2, 3, and 4 nC) in Table 2. The cathode radii in Table 2 were experimentally found to minimize the measured emittance. The scaling procedure and Fig. 9 are used for the compensated space-charge-induced emittances and $\varepsilon_{\text{theory}}$ is found using Eq. (51). We see reasonable (on the order of 20%) agreement. The main conclusion we can form is that the residual space-charge-induced emittance is smaller than the rf-induced emittance, but not negligible. We also see that the additional emittance growth from having a smaller cathode radius results from rf-induced emittance from the growth to a larger beam radius and not from the space-charge-induced emittance.

Because the emittance is dominated by the rf fields, we would have fairly good agreement with some variation in the space-charge-induced emittances (perhaps up to a factor of 2), but the agreement does indicate that the model presented in this paper is consistent with both simulations and experimental data. Unfortunately the experimental data is complicated by additional effects. At higher charges, there can be emittance blow up from transverse wake fields in the accelerating cavities.[21] This can be seen by comparing the 5 nC Gaussian simulation to the 5 nC clipped-Gaussian measurement in Tables 1 and 2. Also, at lower

charges, there is a greater difference between the axially integrated and slice emittances.[10] This difference affects the emittance measurement, and the instantaneous distribution at the peak of the bunch is measured instead.[23] Again comparing Tables 1 and 2, we see a smaller measured emittance than predicted by the simulations at 1 nC. In addition, the experimental uncertainty was about 2 π mm mrad for the measurements.

We will not compare the results of the model for the compensated space-charge-induced emittance and Eq. (51) to the results of either the second short-pulse photoinjector designed to use this compensation scheme, the Advanced Free-Electron Laser at Los Alamos,[8] or the 433 MHz long-pulse photoinjector at Boeing Aircraft Company.[20] The compensation in the Advanced Free-Electron Laser was designed to minimize the slice emittance and not the rms emittance which makes this analysis irrelevant. The Boeing photoinjector is a long-pulse machine; the beam is roughly as long as its diameter as it leaves the cathode. Because particles at different longitudinal positions along the bunch will experience difference long- and short-bunch histories, there will be additional emittance growth mechanisms not included in this model. Note that the residual emittance growth from the mechanism described in this paper would probably be smaller for a long-pulse, low-current machine and that it is quite possible the emittance growth from the additional mechanisms are also

TABLE 1: Summary of PARMELA simulations

Charge	Current	Cathode Radius	Distribution	Emittance	Rotated Field
1.0 nC	130 A	3 mm	Clipped Gaussian	5.5 π mm mrad	quadrupole
5.0	290	5	Flat-top	5.25	none
5.0	300	5	Gaussian	6.5	none
5.0	300	5	Gaussian	10.0	quadrupole
5.0	310	5	Clipped Gaussian	8.0	quadrupole
5.0	330	6	Gaussian	8.0	none
5.0	320	6	Flat-top	6.8	none

TABLE 2: Comparison of Eq. (48) and experimental fit. Units for emittances are π mm mrad.

Charge	Cathode Radius	Current	η	ε_{sc}	$\varepsilon_{\text{theory}}$	$\varepsilon_{\text{meas}}$
1.0	3 mm	130 A	0.86	2.2	4.4	3.5
2.0	4	200	0.75	4.0	7.2	5.2
3.0	4	250	0.94	4.0	8.4	7.0
4.0	4	290	1.08	4.0	9.5	8.9
5.0	5	330	0.79	6.4	11.6	11.6

small enough to lead to a smaller overall emittance than from a short-pulse photoinjector for the same bunch charge. However, bunch compression would be subsequently required to regain the peak current and beam brightness of the short-pulse devices. Also note that the rf frequency for a long-pulse photoinjector would have to be relatively long to avoid excessive rf-induced emittance growth.

As a final check on Eq. (51) we can calculate the optimum cathode radius as a function of current. By differentiating Eq. (51) we find that the optimum cathode radius satisfies

$$0 = 4r^3\hat{\varepsilon}^2(\eta) + 4c_1\left(r + c_2\frac{I}{r}\right)^3\left(1 - c_2\frac{I}{r^2}\right), \tag{52}$$

The optimum radii for 1, 2, 3, 4, and 5 nC are 2.8, 3.4, 3.8, 4.1 and 4.4 mm respectively (compare with Table 2). This is in fair agreement with the experimental findings, and provides additional confidence in Eq. (51) and the results in Section 4.

6 CONCLUSION

We have analyzed an emittance reduction scheme which uses only a simple time-independent lens. This technique can reduce the space-charge-induced emittance growth in a photoinjector by up to an order of magnitude. Although this technique has been discussed previously and experimentally verified, there has been no mechanism to estimate the residual emittance left over after the compensation. This paper included an analytic model which demonstrated where the residual emittance originates from and a numerical model which gave normalized quantitative results concerning the residual emittance. Use of the normalized results and scaling laws can quickly indicate what are the optimal photoinjector design parameters for the desired bunch parameters. Although this technique is used here for electron beams in a photoinjector, it can be generalized to other Hamiltonian systems where one wants to eliminate nonthermal correlations introduced by a nonlinear force.

The mechanism of the compensation technique can be understood with simple analytic models. We examined phase-space plots from an actual photoinjector and determined that the residual emittance left after compensation is dominated by the physics associated with the long-beam regime. Using a numerical model of this regime, we calculated universal residual emittance curves, which led to an emittance-versus-gradient plot for a typical cathode-to-lens spacing. We learned that the residual emittance is small if the beam stays laminar, and increases quickly if the beam's phase space bifurcates. We also found that the residual space-charge-induced emittance growth is minimized for a given current if the current density off the cathode is about 15 E^2 A/cm^2 where E is the accelerating gradient in MV/m. In addition, as predicted in the simple analytic model, compensation only occurs if the linear focusing element lies sufficiently close to the cathode. As a result, the minimum emittance does not occur for the maximum possible gradient until the gradient is so high that the uncompensated emittance is lower than the compensated emittance at the lower gradient. Assuming that the rf-induced and the residual space-charge-induced emittance growths are uncorrelated, we predicted the overall rms emittance would have the scaling used in Eq. (51). Eq. (51) was then shown to be consistent with both the APEX simulations and the measured data. This agreement demonstrates that the model for the

compensated space-charge-induced emittance is reasonably accurate. Using this model and Kim's equation for the rf-induced emittance, we suspect that it is possible to have rms emittances roughly one-half those at APEX by eliminating the nonlinear rf fields. This model also accurately predicted optimum experimental cathode radii.

The rf-induced emittance growth in a photoinjector (Eq. (2)) increases linearly with gradient and quadratically with frequency. The main reason to go to higher frequency and gradient is to reduce the space-charge-induced emittance growth. Use of the compensation technique allows operation of lower frequency and gradient photoinjectors with lower overall emittance growth for a given peak current.

ACKNOWLEDGEMENTS

The author thanks P.G. O'Shea, K.-J. Kim, R.L. Sheffield, R. Warren, M.E. Jones, and L.E. Thode for useful discussions. He also thanks Dr. O'Shea and D.W. Feldman for providing the experimental data.

APPENDIX

In this Appendix, we will show that under some circumstances the compensation can be simultaneously made for both the nonlinearities resulting from the short-bunch regime and the long-bunch regime with a single infinitely thin lens. Then we will examine what happens if multiple thin lenses (or a thick lens) are used.

Although the beam is in general accelerating, it is possible to construct an instantaneous inertial frame of reference comoving with the beam. If the acceleration is sufficiently small compared to the beam length so retardation effects do not create relative beam motion and variations in density, then the transverse motion obeys

$$\frac{d^2r}{dt_b^2} = \lambda_b(\rho, \zeta) \,, \tag{A1}$$

where t_b is the proper time in the instantaneous beam frame of reference and λ_b is the force times the electronic charge over its mass in that frame. Note that λ_b differs from the normalized force Λ_b defined in Eq. (4) by the factor $1/\gamma^3\beta^2c^2$. The laboratory frame is related to the beam frame by

$$\gamma\beta c dt_b = dz \,. \tag{A2}$$

Using the relations

$$\lambda_b = E_{rb}\frac{e}{m} \,, \tag{A3}$$

$$\lambda_l = \frac{1}{\gamma^2}E_{rl}\frac{e}{m} \,, \tag{A4}$$

and

$$E_{rl} = \gamma E_{rb} \,, \tag{A5}$$

where the l subscript refers to the laboratory frame, we see that the transverse equation of motion becomes

$$\gamma\beta c \frac{d}{dz}\left(\gamma\beta c \frac{dr}{dz}\right) = \lambda_b = \frac{eE_{rl}}{\gamma m} = \gamma\lambda_l \,. \tag{A6}$$

We can integrate Eq. (A6) once to yield

$$\gamma\beta c \frac{dr}{dz} = \int_0^z \frac{dz'}{\beta c} dz' + r'_o \gamma_o \beta_o c \tag{A7}$$

where the o subscript refers to the variables' values at $z = 0$. Integrating again gives

$$r = r_o + r'_o \gamma_o \beta_o \int_0^z \frac{dz'}{\gamma\beta} + \int_0^z \frac{dz'}{\gamma\beta c} \int_0^{z'} \frac{d\hat{z}}{\beta c} \lambda_l \,. \tag{A8}$$

Here the γ's, β's, and λ_l's are functions of the dummy integration variable z' or $\hat{z}$ that they are associated with under the integral. Just before the lens at $z = z_l$ we have

$$r_{bl} = r_o + r'_o \gamma_o \beta_o \int_0^{z_l} \frac{dz'}{\gamma\beta} + \int_0^{z_l} \frac{dz'}{\gamma\beta c} \int_0^{z'} \frac{d\hat{z}}{\beta c} \lambda_l \,. \tag{A9}$$

and

$$r'_{bl} = \frac{1}{\gamma\beta c} \int_0^{z_l} \frac{dz'}{\beta c} \lambda_l + r'_o \frac{\gamma_o \beta_o}{\gamma\beta} \,, \tag{A10}$$

using bl to mean before lens. We will assume a linear lens with a focal length of α_l. At a position z_d beyond the lens, we find

$$r = r_o + r'_o \gamma_o \beta_o \int_0^{z_l} \frac{dz'}{\gamma\beta} + \int_0^{z_l+z_d} \frac{dz'}{\gamma\beta c} \int_0^{z'} \frac{d\hat{z}}{\beta c} \lambda_l + r'_o \gamma_o \beta_o \int_{z_l}^{z_l+z_d} \frac{dz'}{\gamma\beta}$$

$$- \alpha_l \gamma_l \beta_l \int_{z_l}^{z_l+z_d} \frac{dz'}{\gamma\beta} \left(r_o + r'_o \gamma_o \beta_o \int_0^{z_l} \frac{dz'}{\gamma\beta} + \int_0^{z_l} \frac{dz'}{\gamma\beta c} \int_0^{z'} \frac{d\hat{z}}{\beta c} \lambda_l \right) \,, \tag{A11}$$

and

$$r' = \frac{1}{\gamma\beta c}\int_0^{z_l+z_d} \frac{dz'}{\beta c}\lambda_l + r'_o\frac{\gamma_o\beta_o}{\gamma\beta}$$

$$-\alpha_l\frac{\gamma_l\beta_l}{\gamma\beta}\left(r_o + r'_o\gamma_o\beta_o\int_0^{z_l}\frac{dz'}{\gamma\beta} + \int_0^{z_l}\frac{dz'}{\gamma\beta c}\int_0^{z'}\frac{d\hat{z}}{\beta c}\lambda_l\right), \tag{A12}$$

where γ_l and β_l are the particles' gamma and beta at the lens position.

At this point, we will make an approximation for the laboratory space-charge force λ_l that is valid in both the short- and long-beam regimes. We will use a form slightly different than Eq. (22) in order to manifest the linear axial force expansion, Eq. (14). The space-charge force will be assumed to be of the form

$$\lambda_l(\rho,\zeta) = \rho\frac{1}{\gamma^2}\left(\Lambda_o k(\rho)e^{-A_r/0.85} + (\Lambda_o + \Lambda'_o\chi)(1-e^{-A_r/0.36})\right) \tag{A13}$$

where Λ_o is given by Eq. (23), $\chi = \zeta - \zeta_o$ (as before), k is some radial function, and Λ'_o is a function of z only describing the linear dependence of the radial field on a particle's displacement from ζ_o.

As before, no emittance at the beam location $z_l + z_d$ means at that location

$$\frac{r'_i}{r_i} = \frac{r'_j}{r_j} \tag{A14}$$

or

$$0 = r_i r'_j - r_j r'_i \tag{A15}$$

for all particles i and j. This in turn requires that the coefficients of the three terms in Eq. (A15) with the factors $k(\rho_i) - k(\rho_j)$, $k(\rho_j)\chi_j - k(\rho_j)\chi_i$, and $\chi_i - \chi_j$ be zero.

We can define the following integrands to simplify the resulting expressions:

$$I_1 = \Lambda_o\left(1 - e^{-A_r/0.36}\right), \tag{A16}$$

$$I_2 = \Lambda_o e^{-A_r/0.85}, \tag{A17}$$

and

$$I_3 = \Lambda'_o\left(1 - e^{-A_r/0.36}\right). \tag{A18}$$

The three equations that must be satisfied are given by

$$(BI - CH) - \alpha_l(EI + BL - CK - FH) = 0, \tag{A19}$$

$$(BG - AH) - \alpha_l(EG + BJ - AK - DH) = 0, \tag{A20}$$

and

$$(CG - AI) - \alpha_l(FG + CJ - AL - DL) = 0\,, \tag{A21}$$

where

$$A = r_o + r'_o\gamma_o\beta_o \int_0^{z_l} \frac{dz'}{\gamma\beta} + \int_0^{z_l+z_d} \frac{dz'}{\gamma\beta c} \int_0^{z'} \frac{d\hat{z}}{\gamma^2\beta c} I_1 + r'_o\gamma_o\beta_o \int_{z_l}^{z_l+z_d} \frac{dz'}{\gamma\beta}\,, \tag{A22}$$

$$B = \int_0^{z_l+z_d} \frac{dz'}{\gamma\beta c} \int_0^{z'} \frac{d\hat{z}}{\gamma^2\beta c} I_2\,, \tag{A23}$$

$$C = \int_0^{z_l+z_d} \frac{dz'}{\gamma\beta c} \int_0^{z'} \frac{d\hat{z}}{\gamma^2\beta c} I_3\,, \tag{A24}$$

$$D = \gamma_l\beta_l \int_{z_l}^{z_l+z_d} \frac{dz'}{\gamma\beta} \left(r_o + r'_o\gamma_o\beta_o \int_0^{z_l} \frac{dz'}{\gamma\beta} + \int_0^{z_l} \frac{dz'}{\gamma\beta c} \int_0^{z'} \frac{d\hat{z}}{\gamma^2\beta c} I_1 \right)\,, \tag{A25}$$

$$E = \gamma_l\beta_l \int_{z_l}^{z_l+z_d} \frac{dz'}{\gamma\beta} \left(\int_0^{z_l} \frac{dz'}{\gamma\beta c} \int_0^{z'} \frac{d\hat{z}}{\gamma^2\beta c} I_2 \right)\,, \tag{A26}$$

$$F = \gamma_l\beta_l \int_{z_l}^{z_l+z_d} \frac{dz'}{\gamma\beta} \left(\int_0^{z_l} \frac{dz'}{\gamma\beta c} \int_0^{z'} \frac{d\hat{z}}{\gamma^2\beta c} I_3 \right)\,, \tag{A27}$$

$$G = \frac{1}{\gamma\beta} \int_0^{z_l+z_d} \frac{dz'}{\gamma^2\beta c} I_1 + r'_o \frac{\gamma_o\beta_o}{\gamma\beta}\,, \tag{A28}$$

$$H = \frac{1}{\gamma\beta} \int_0^{z_l+z_d} \frac{dz'}{\gamma^2\beta c} I_2\,, \tag{A29}$$

$$I = \frac{1}{\gamma\beta} \int_0^{z_l+z_d} \frac{dz'}{\gamma^2\beta c} I_3\,, \tag{A30}$$

$$J = \frac{\gamma_l \beta_l}{\gamma \beta}\left(r_o + r'_o \gamma_o \beta_o \int_0^{z_l} \frac{dz'}{\gamma\beta} + \int_0^{z_l} \frac{dz'}{\gamma\beta c} \int_0^{z'} \frac{d\hat{z}}{\gamma^2 \beta c} I_1 \right) , \tag{A31}$$

$$K = \frac{\gamma_l \beta_l}{\gamma \beta}\left(\int_0^{z_l} \frac{dz'}{\gamma\beta c} + \int_0^{z'} \frac{d\hat{z}}{\gamma^2 \beta c} I_2 \right) , \tag{A32}$$

and

$$L = \frac{\gamma_l \beta_l}{\gamma \beta}\left(\int_0^{z_l} \frac{dz'}{\gamma\beta c} + \int_0^{z'} \frac{d\hat{z}}{\gamma^2 \beta c} I_3 \right) , \tag{A33}$$

Although Eqs. (A19)–(A21) are nonlinear, they can be satisfied with sufficient number of free variables. In particular, if the accelerating gradient can be tailored, the integrals can be adjusted to give a solution. In that case, the beam is compensated in both the short- and long-bunch regimes.

To show that a solution can exist, let's consider for example a beam line with made up of drifts and sections with accelerating fields so high that the acceleration can be considered to take place over an infinitesimal distance. Say the beam line starts with a drift l_1 with a beam energy of $\gamma_1 m_o c^2$ followed by a sudden acceleration to an energy of $\gamma_2 m_o c^2$. The beam drifts at this energy for a distance l_2 and then is suddenly accelerated to an energy of $\gamma_3 m_o c^2$, followed by a final drift of length l_3. Let us assume that the focusing lens is in the middle of the second drift, the integrands in Eqs. (A16)–(A18) are small (after integration compared to the initial beam radius), and the lengths are adjusted such that

$$\frac{l_n}{\gamma_n \beta_n} = 1 \tag{A34}$$

in the units we are using. If we assume that the beam's aspect ratio does not change appreciably within the drifts, we can use the notation $I_{n,m} = I_n(\gamma_m)$ to specify the different integrands along the drifts m. If γ_1 is very close to one and γ_3 is very large, then the integrands $I_{3,1}$ and $I_{2,3}$ vanish and $I_{2,1}$ and $I_{3,3}$ are unity if the current distribution is triangular and if $\Lambda_o = 1$ in our units. For this special case, only A, D, and J are first order and the rest are higher order. The coefficient for $k(\rho_i)\chi_j - k(\rho_j)\chi_i$ (Eq. (A19)) becomes second order and vanishes and Eqs. (A20) and (A21) lead to

$$2 = 3I_{3,2} - \frac{I_{2,2}}{\gamma_2} . \tag{A35}$$

This equation has a solution because we have not specified γ_2; as γ_2 becomes small $I_{3,2}$ approaches, zero and $I_{2,2}$ approaches one and as γ_2 becomes large $I_{3,2}$ approaches one and $I_{2,2}$ approaches zero. The inverse focal length α_l can then be found using either Eq. (A20) or Eq. (A21). Eqs. (A19)–(A21) have been numerically solved for other, realistic photoinjector designs.[13]

An alternative method to simultaneously compensate in the long- and the short-bunch regimes would be to introduce additional thin lenses. Three lenses would lead in general to a quartic equation for the values of the lenses' focal strengths; fortunately, all terms quadratic and higher can be forced to drop out, leaving a simple linear system to solve. The integrals depend on the lenses' strengths because they modify the beam's aspect ratio through focusing, but typically the coupling is sufficiently weak and no problem is introduced.

In real photoinjectors we don't have complete flexibility to tailor the accelerating gradient to some peculiar profile. However, we do have some amount of flexibility to modify the thick lens used for the compensation. The combination of the design of the thick lens and the gradient profile gives enough degrees of freedom to ensure the simultaneous compensation.

REFERENCES

1. B.E. Carlsten, "New photoelectric injector design for the Los Alamos National Laboratory XUV FEL accelerator," *Nucl. Instrum. Methods Phys. Res.*, **A285**, 313 (1989).
2. B.E. Carlsten, J.C. Goldstein, E.J. Pitcher and M.J. Schmitt, "Simulations of APEX accelerator performance in the new nonthermalized photoinjector regime," *Nucl. Instrum. Methods Phys. Res.*, **A331**, 307 (1993).
3. K.T. McDonald, "Design of the laser-driven rf electron gun for the BNL accelerator test facility," Princeton Preprint DOE/ER/3072-43 (1988).
4. K.J. Kim, "Rf and space-charge effects in laser-driven rf electron guns," *Nucl. Instrum. Methods Phys. Res.*, **A275**, 201 (1989).
5. M.E. Jones and B.E. Carlsten, "Space-Charged-Induced Emittance Growth in the Transport of High-Brightness Electron Beams," *IEEE Particle Accelerator Conf.*, Washington, D. C., March 1987, IEEE Cat. No. 87CH2387-9, 1319 (1987).
6. J.S. Fraser, R.L. Sheffield, E.R. Gray, P.M. Giles, R.W. Springer, and V. A. Loebs, "Photocathodes in accelerator applications," *IEEE Particle Accelerator Conf.*, Washington, D. C., March 1987, IEEE Cat. No. 87CH2387-9, 1391 (1987).
7. B.E. Carlsten, L.M. Young, M.J. Browman, H. Takeda, D.W. Feldman, P.G. O'Shea and A.H. Lumpkin, "INEX simulations of experimentally measured accelerator performance at the Los Alamos HIBAF facility," *Nucl. Instrum. Methods Phys. Res.*, **A304**, 587 (1991).
8. R.L. Sheffield, R.H. Austin, K.D.C. Chan, S.M. Gierman, J.M. Kinross-Wright, S.H. Kong, D.C. Nguyen, S.J. Russell and C.A. Timmer, "Performance of the high brightness linac for the Advanced Free Electron Laser Initiative at Los Alamos," submitted to the *Proc. 15th Intern. Free Elect. Laser Conf.*, The Hague, The Netherlands, August 1993.
9. K. Batchelor, I. Ben-Zvi, R.C. Fernow, J. Fischer, A.S. Fisher, J. Gallardo, G. Ingold, H.G. Kirk, K.P. Leung, R. Malone, I. Pogorelsky, T. Srinivasan-Rao, J. Rogers, T. Tsang, J. Sheehan, S. Ule, M. Woodle, J. Xie, R. S. Zhang, L.Y. Lin, K.T. McDonald, D.P. Russell, C.M. Hung, and X.J. Wang, "Performance of the Brookhaven photocathode rf gun," *Nucl. Instrum. Methods Phys. Res.*, **A318**, 372 (1991).
10. B.E. Carlsten, L.M. Young, M.E. Jones, L.E. Thode, A.H. Lumpkin, D.W. Feldman, R.B. Feldman, B. Blind, M.J. Browman and P.G. O'Shea, "Design and Analysis of Experimental Performance of the Los Alamos HIBAF Facility Accelerator Using the INEX Computer Model," *IEEE Journ. Quant. Elect.*, **27**(12), 2580(1991).
11. L. Serafini, R. Rivolta, L. Terzoli and C. Pagani, "Rf gun emittance correction using unsymmetrical rf cavities," *Nucl. Instrum. Methods Phys. Res.*, **A318**, 275 (1991).
12. G. Gao, Laboratoire Accelerator Linear, private communication.

13. B.E. Carlsten, "Photoelectric Injector Design Code," *IEEE Particle Accelerator Conf.*, Chicago, IL., IEEE Cat. No. 89CH2669-0, 313 (1989).

14. P.F. Loschialpo, "Effect on nonlinear space charge and magnetic forces on electron beams focused by a solenoid lens," Ph.D. thesis, University of Maryland (1984).

15. S.V. Benson, W.S. Fann, B.A. Hooper, J.M.J. Madey, E.B. Szarmes, B. Richman, and L. Vintro, "A review of the Stanford Mark III infrared FEL program," *Nucl. Instrum. Methods Phys. Res.*, **A296**, 110 (1990).

16. B.E. Carlsten, B.D. McVey and R.L. Sheffield, "Photoelectric injector designs at Los Alamos National Laboratory," *Proc. of the Bendor Workshop on Short-Pulse, High-Current Cathodes*, Editions Frontieres 165 (1990).

17. H. Bateman, *Partial Differential Equations of Mathematical Physics* (Cambridge University Press, Cambridge 1969), Chap. 8, pp. 421–425.

18. L.M. Young, Los Alamos National Laboratory, private communication.

19. B.E. Carlsten, L.M. Young, M.E. Jones, B. Blind, E.M. Svaton, K.C. D. Chan, and L.E. Thode, "Accelerator design and calculated performance of the Los Alamos HIBAF facility," *Nucl. Instrum Meth. Phys. Res.*, **A296**, 687 (1990).

20. H. Takeda and D. Dowell, "Modeling the APLE injector solenoid magnetic field with the Biot-Savart law," *Nucl. Instrum Meth. Phys. Res.*, **A331**, 384 (1993).

21. P.G. O'Shea, S.C. Bender, B.E. Carlsten, J.W. Early, D.W. Feldman, A.H. Lumpkin, R.B. Feldman, J.C. Goldstein, K.F. McKenna, R. Martineau, E.J. Pitcher, M.J. Schmitt, W.E. Stein, M.D. Wilke and T.J. Zaugg, "Performance of the APEX free-electron laser at Los Alamos National Laboratory," *Nucl. Instrum Meth. Phys. Res.*, **A331**, 62 (1993).

22. P.G. O'Shea, Los Alamos National Laboratory, private communication.

23. B.E. Carlsten, J.C. Goldstein, P.G. O'Shea and E.J. Pitcher, "Measuring emittance of nonthermalized electron beams from photoinjectors," *Nucl. Instrum Meth. Phys. Res.*, **A331**, 791 (1993).